



NTNU – Trondheim
Norwegian University of
Science and Technology

An experimental study of a transversely forced round jet

Michael Amund Enger
Dalton

Master of Science in Mechanical Engineering

Submission date: June 2014

Supervisor: James Dawson, EPT

Norwegian University of Science and Technology
Department of Energy and Process Engineering

EPT-M-2014-22

MASTER THESIS

for

Michael Dalton

Spring 2014

An experimental study of a transversely forced round jet*En eksperimentell studie av en tværrforstyrret rund stråle***Background and objective**

Self-excited thermo-acoustic instabilities are a well-known design problem for low-emission gas turbine combustors for power generation and propulsion. In gas turbines, the combustion chamber is usually annular in design with up to 20 fuel injectors arranged around the circumference. Low-emission technologies aim to operate fuel lean and premixed but this often leads to unwanted pressure oscillations caused by acoustic waves travelling around the annulus constructively interacting with the unsteady heat release rate of the flames. Recent experiments have shown that flames located at the pressure nodes undergo strong transverse, anti-symmetric motions, which were not previously observed. The aim of this project is to assemble an apparatus for transverse forcing of a jet in order to elucidate the sensitivity and dynamics of shear layers (where flames are normally stabilised) can be investigated in more detail and under well-controlled laboratory conditions.

The following tasks are to be considered:

1. Build, test, and calibrate a simple apparatus based on calculations from recent project work.
2. Carry out velocity measurements in the near field of a round jet subjected to transverse acoustic forcing using Particle Image Velocimetry (PIV).
3. Process and analyse the data.

Within 14 days of receiving the written text on the master thesis, the candidate shall submit a research plan for his project to the department.

When the thesis is evaluated, emphasis is put on processing of the results, and that they are presented in tabular and/or graphic form in a clear manner, and that they are analyzed carefully.

The thesis should be formulated as a research report with summary both in English and Norwegian, conclusion; literature references, table of contents etc. During the preparation of the text, the candidate should make an effort to produce a well-structured and easily readable report. In order to ease the evaluation of the thesis, it is important that the cross-references are correct. In the making of the report, strong emphasis should be placed on both a thorough discussion of the results and an orderly presentation.

The candidate is requested to initiate and keep close contact with his/her academic supervisor(s) throughout the working period. The candidate must follow the rules and regulations of NTNU as well as passive directions given by the Department of Energy and Process Engineering.


Risk assessment of the candidate's work shall be carried out according to the department's procedures. The risk assessment must be documented and included as part of the final report. Events related to the candidate's work adversely affecting the health, safety or security, must be documented and included as part of the final report. If the documentation on risk assessment represents a large number of pages, the full version is to be submitted electronically to the supervisor and an excerpt is included in the report.

Pursuant to "Regulations concerning the supplementary provisions to the technology study program/Master of Science" at NTNU §20, the Department reserves the permission to utilize all the results and data for teaching and research purposes as well as in future publications.

The final report is to be submitted digitally in DAIM. An executive summary of the thesis including title, student's name, supervisor's name, year, department name, and NTNU's logo and name, shall be submitted to the department as a separate pdf file. Based on an agreement with the supervisor, the final report and other material and documents may be given to the supervisor in digital format.

- Work to be done in lab (Water power lab, Fluids engineering lab, Thermal engineering lab)
 Field work

Department of Energy and Process Engineering, 14. January 2014


Olav Bolland
Department Head


James Dawson
Academic Supervisor

Acknowledgements

I would like to offer a very special thanks to Prof. James Dawson, my supervisor, who's help has been invaluable. Without him my master thesis would likely have been a lot less interesting.

A thank you goes to Philip, who's programming skills saved me a great deal of trouble when preparing data for postprocessing.

A special thanks to Atle Jensen, professor at UiO, who sparked my interest for fluid dynamics.

And finally, thanks to all friends and family, for their support throughout these years.

Contents

1 Introduction	2
2 Background	3
2.1 Standing waves	3
2.2: Helmholtz equation	3
2.3 Theoretical eigenmodes of a box	5
2.4 Transversely forced jets	6
2.5 Fourier transforms and spectral analysis	8
3 Methods	9
3.1 Software used	9
3.2 Simulations	9
3.3 Acoustic mapping	10
3.3.1 General setup	10
3.3.2 Microphone calibration	12
3.3.3 Frequency Sweep and Mode shape	12
3.4 Jet	13
4 Results	15
4.1 Simulations	15
4.2 Frequency sweeps	17
4.3 Mode locations and shapes	22
4.4 Forced Jet	31
5. Conclusion	42
6. Bibliography	43
Appendix	44
A.1 Z-axis plots with discrepancies	44
A.2 Pictures of the box and setup	47

1 Introduction

It has been well established that an interaction between combustion and acoustics can produce self-sustained acoustic oscillations, for example in so called Rijke tubes, where a mesh in a pipe interacts with a flame to produce a tone [1]. This was discovered already in 1859. In recent years, thermo-acoustic instabilities have been a hot research topic, mainly because of a drive for more environmentally friendly gas turbines. Reducing NO_x and CO gas emissions and increasing efficiency means lean combustion, but this makes the combustion chamber of the gas turbine more prone to self-induced thermo-acoustic instabilities. These thermo-acoustic instabilities are not fully understood, and are detrimental to both the efficiency and structural integrity of a gas turbine.

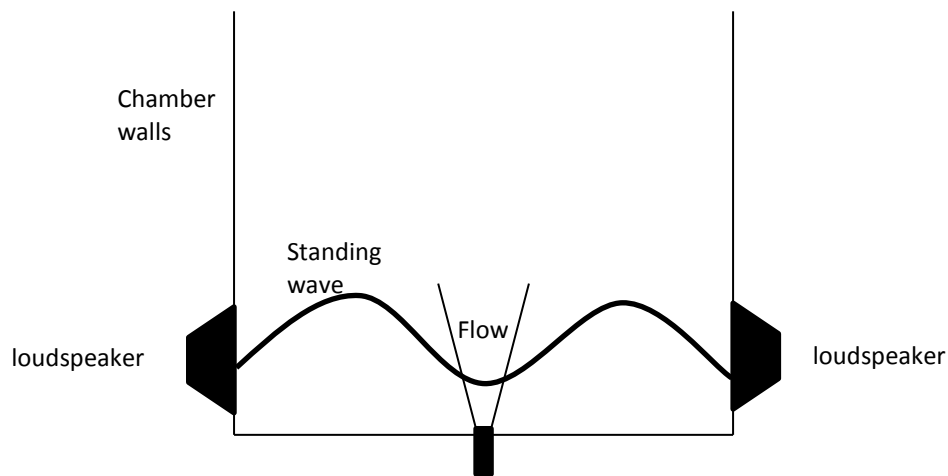


[Fig 1] Example of acoustically forced flow

Though the typical combustion chamber is an annulus where both standing waves and travelling waves occur, the standing waves are often researched by themselves in box-shaped acoustic chambers ([2], [3]). A setup may look something like figure 1, where loudspeakers on each side of a chamber interact with some sort of flow, e.g. a jet.

Typically, the flow studied is a combusting flow. This thesis however, seeks to isolate the acoustic/fluid flow interaction, without the added effects of combustion. Using a setup like that in figure 1, this thesis encompasses work done to characterise an acoustic chamber for experiments, and to carry out measurements of a forced jet. Of special interest are the areas inbetween the acoustic pressure node and antinode, where there is very little data available. Though so-called PIV (Particle Image Velocimetry) measurements were planned, there was unfortunately not enough time to carry them out. The images taken for processing are however presented, and these provide new insight into acoustically forced flows.

2 Background

2.1 Standing waves

Acoustic standing waves form when two travelling waves travelling in opposite directions interfere constructively, giving rise to a stationary, or standing, wave. They are familiar to most, as their occurrence is commonly associated with acoustic resonance, a property used in e.g. musical instruments.

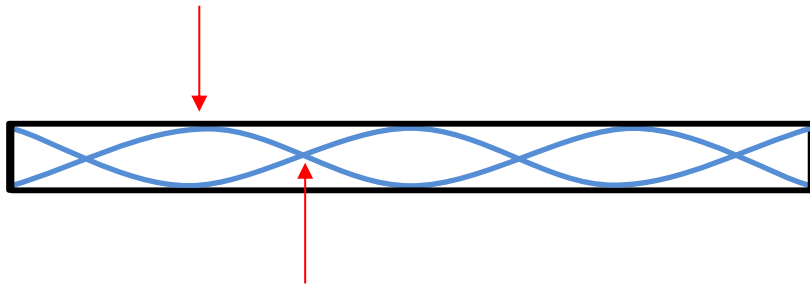


[Fig 2] Standing waves in tube closed at both ends

The following equation describes the one-dimensional resonator's resonant frequencies, or eigenfrequencies;

$$f = \frac{nc_0}{2L} \quad (1)$$

where L is the length of the tube, n the mode number, c_0 is the speed of sound, and f the forcing frequency. Figure 2 shows a standing wave in a tube with closed ends. Here, the mode number would be 4. Figure 2 shows the pressure distribution of the standing wave; for velocity nodes and antinodes are switched. When referring to nodes and antinodes in this thesis, pressure nodes and antinodes are being referred to unless otherwise is stated specifically.

2.2: Helmholtz equation

The Helmholtz equation is used when solving for the resonance modes in the chamber, and describes the pressure variation in a harmonic sound field. Assuming first that the fluid is quiescent, and that variables, e.g. velocity v may be split up into a mean V and a perturbation v' , the equations of motion can be simplified to

$$\rho_0 \frac{\partial v'}{\partial t} + \nabla p' = 0 \quad (2)$$

$$\frac{\partial \rho'}{\partial t} + \rho_0 \nabla \cdot \mathbf{v}' = 0 \quad (3)$$

with

$$\frac{\partial s'}{\partial t} = 0 \quad (4)$$

As given in *An Introduction to Acoustics* [4] p. 18. Equation 4 can be used to simplify the constitutive relation

$$c^2 = \left(\frac{\partial p}{\partial \rho} \right)_s \quad (5)$$

Into

$$p' = c_0^2 \rho' \quad (6)$$

If the time derivative of equation 3 is taken, and then subtracted from the divergence of equation 2, \mathbf{v}' is eliminated to give

$$\nabla^2 p' - \frac{\partial^2 \rho'}{\partial t^2} = 0 \quad (7)$$

Using 6 to eliminate ρ' gives

$$\nabla^2 p' - \frac{1}{c^2} \frac{\partial^2 p'}{\partial t^2} = 0 \quad (8)$$

which is the wave equation for pressure. The sound wave is then assumed to be split into partial waves with a harmonic time dependency, and thus the pressure and velocity in the sound field can be described by

$$p(\mathbf{r}, t) = \text{Re}\{\hat{p}(\mathbf{r}) \cdot e^{i\omega t}\} \quad (9)$$

$$\mathbf{v}(\mathbf{r}, t) = \text{Re}\{\hat{\mathbf{v}}(\mathbf{r}) \cdot e^{i\omega t}\} \quad (10)$$

Re signifies the real value taken of the expression, and $\hat{\mathbf{v}}(\mathbf{r})$ and $\hat{p}(\mathbf{r})$ are complex amplitudes.

Using (9) the wave equation can with be simplified into

$$\nabla^2 p' + k^2 p' = 0 \quad (11)$$

which is the well-known Helmholtz equation. Noting that this is an eigenvalue problem, the resulting solution for a given set of boundaries will be a set of eigenfunctions that describe the pressure field for a resonance mode. Contained in the eigenfunctions are also the eigenfrequencies, which are the resonant frequencies. This is what COMSOL's acoustics eigenfrequency module solves for in a model.

2.3 Theoretical eigenmodes of a box

The calculation of theoretical box modes can be derived from the Helmholtz equation. Following the procedure given in [5, pp. 110-111], the Helmholtz equation is given by:

$$\nabla^2 p' + k^2 p' = 0 \quad (12)$$

where k is the wavenumber. Assuming infinitely stiff boundary surfaces and no other energy losses, the eigenfunctions for the pressure will be given by

$$p'_{n_x n_y n_z}(x, y, z) = C \cdot \cos(k_x x) \cdot \cos(k_y y) \cdot \cos(k_z z) \quad (13)$$

where C is a constant. The eigenvalues for the wave number are given by

$$k_n^2 = k_x^2 + k_y^2 + k_z^2 = \left(\frac{n_x \pi}{L_x}\right)^2 + \left(\frac{n_y \pi}{L_y}\right)^2 + \left(\frac{n_z \pi}{L_z}\right)^2 \quad (14)$$

And the corresponding eigenfrequencies by

$$f_{n_x n_y n_z} = \frac{c_0}{2} \sqrt{\left(\frac{n_x}{L_x}\right)^2 + \left(\frac{n_y}{L_y}\right)^2 + \left(\frac{n_z}{L_z}\right)^2} \quad (15)$$

Where c_0 is the speed of sound, n_i the mode number in the corresponding dimension, and L_i the length in the corresponding dimension. Modes in which only one mode number is nonzero are called axial modes, while two nonzero mode numbers gives a tangential mode, and three nonzero mode numbers gives an oblique mode. Axial modes are equivalent to one-dimensional standing waves in a tube, while in tangential modes and oblique modes have standing waves in two and three dimensions, respectively.

Though the acoustic chamber differs from a room in that there is necessarily an inlet and outlet complicating the acoustic resonant response, a simplified model can be used for reasonable estimates. If the inlet for the jet flow is neglected and the outlet is assumed to be

an entire removed wall at the top, the established theory for eigenmodes of a room can be modified to give an approximate mathematical model.

$$f_{n_x n_y n_z} = \frac{c_0}{2} \sqrt{\left(\frac{n_x}{L_x}\right)^2 + \left(\frac{n_y}{L_y}\right)^2 + \left(\frac{2n_z - 1}{L_z}\right)^2} \quad (16)$$

It should be noted that no pure axial modes are expected to exist in the x and y direction. This is due to that the pressure would have to be constant along the walls that are in contact with open air on one side, and closed on the other. Since an open end must be a pressure node, and a closed end must be a pressure antinode, the pressure must vary over the wall (or there be a discontinuity). Thus, any mode $n_z=0$ cannot exist.

This thesis using the following notation for eigenmodes: (X,Y,Z) , where X, Y and Z are the mode numbers in their respective dimensions.

2.4 Transversely forced jets

An unforced axisymmetric jet may look something like figure 3. There is a core that remains undisturbed for a couple of jet diameters, before it breaks down into vortices, before breaking further down into turbulence.

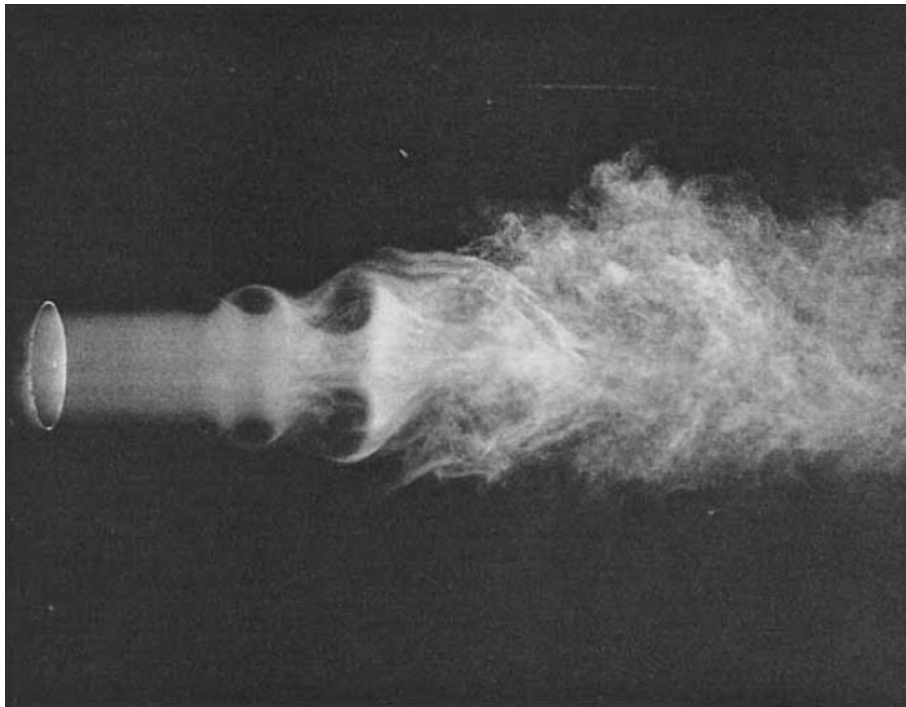


[Fig 3] Spark photograph of a 1 in. fog jet, $Re=10500$. From Crow and Champagne, “Orderly structure in jet turbulence”, Plate 4, figure 6a [6]

It has been well established that acoustic waves can have a significant impact on fluid flow. A jet flow subjected to periodic instabilities (that need not be of an acoustic nature), will be modulated (**e.g.** [7]). Most experiments dealing with transversely forced flow in an acoustic field work with either a pressure node or antinode ([2], [3], [8], [9]).

For example, a jet placed in the pressure antinode of a sufficiently powerful standing acoustic field will form symmetric vortices. The effect is equivalent to an axial forcing (in the direction of the jet) that can be seen in figure 4. If the jet is placed in a pressure node (i.e. anti-symmetric forcing) produces anti-symmetric modulation of the jet.

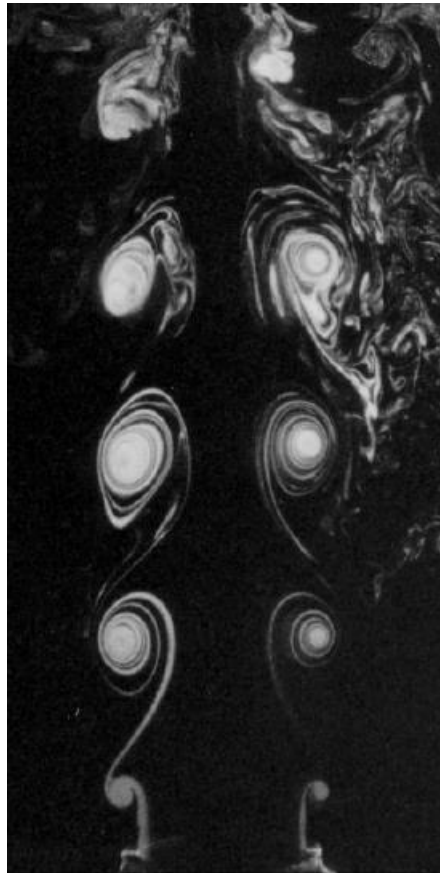
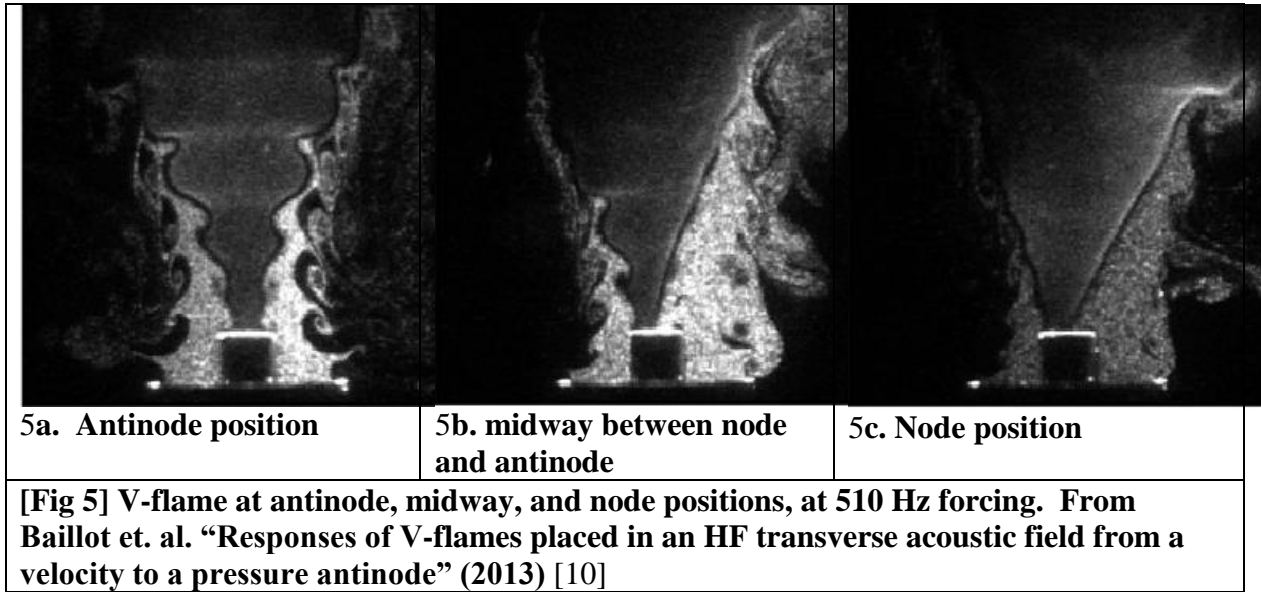


**[Fig 4] axially forced jet at $Re=10000$.
From Parekh et. al., “Bifurcating Jets at
High Reynold’s number” (1988) [13]**

Additionally, Baillot ([10]) has done some investigation of a flame between a node and an antinode. The flame originated from a jet with a bluff body in the centre however, so the overall flow is quite different from the previous pictures. Fig 5 shows a selection of these pictures. It is difficult to make out clear vortex patterns outside of the antinode position, but it is clear that vortices are present, and that the flame “leans” to one side as it is moved to the node position.



2.5 Fourier transforms and spectral analysis

The Fourier transform is a well-established mathematical transformation that transforms a function from the time domain to the frequency domain. The Fourier transform $\hat{f}(w)$ is given as follows (from [11] p.519-525),

$$\hat{f}(w) = \frac{1}{\sqrt{2\pi}} \int_{-\infty}^{\infty} f(x) e^{-iwx} dx \quad (17)$$

And its counterpart, the inverse transform

$$f(x) = \frac{1}{\sqrt{2\pi}} \int_{-\infty}^{\infty} \hat{f}(w) e^{iwx} dw \quad (18)$$

However, the above is used for functions and not sampled data, where information is only available at discrete points. For this, there is the Discrete Fourier Transform (DFT), where a signal in the form of N (equally spaced) discrete samples, given by $[f_0 \cdots f_{N-1}]$, is transformed into a vector $\hat{f} = [\hat{f}_0 \cdots \hat{f}_{N-1}]$

$$\hat{f}_n = \sum_{k=0}^{N-1} f(x_k) e^{-inx_k} \quad (19)$$

\hat{f} is the frequency spectrum of the signal. Each element \hat{f}_n contains information on the phase and amplitude of a sinusoidal component of the original signal. The sinusoidal component has a frequency given by $\frac{nf_s}{N}$ where f_s is the sampling frequency .

Taking the complex conjugate of each element will give the power \hat{P}_n of each sinusoidal component, and taking the square root of the power will give the amplitude, i.e.

$$\hat{P}_n = \hat{f}_n \times \text{conj}(\hat{f}_n) \quad (20)$$

$$\hat{A}_n = \sqrt{\hat{f}_n \times \text{conj}(\hat{f}_n)} \quad (21)$$

When frequency plotted against either of these will tell which frequencies appear in the original signal, and how strong they are. A plot of frequency versus power is the power spectral density.

3 Methods

3.1 Software used

Matlab r2011b has been used extensively for post-processing all microphone data. Scripts used can be found in the attached zip file, or provided upon request.

COMSOL multiphysics 4.3b is the finite element/finite volume solver used for the acoustic simulations.

Labview 2013 was used to capture microphone data for all experiments.

Davis version 8, a PIV program, was used to capture footage (including synchronising camera and laser).

3.2 Simulations

A COMSOL model was used to evaluate the eigenmodes of the box. Based on previous work [12] with some slight modifications, it consists of a volume representing the box, and a volume representing the surrounding atmosphere. The atmosphere is surrounded by perfectly matched layers (PMLs), which approximate an infinite boundary by damping out any waves travelling through it.

The mesh inside the box was set to be a free tetrahedral with a maximum size of 0.023m. The atmosphere was set to a COMSOL preset, ‘‘Coarse’’. This gives good accuracy for predicting

the frequency of emerging modes, but though higher order mode shapes can show some sensitivity to mesh density. This required additional mesh refinement when collecting data for the shortest box configuration, where the mesh was set to a free tetrahedral of maximum size 0.016m. The interior of the box and its lip were set to be hard acoustic boundaries, and the outside of the PMLs were set to reference atmospheric pressure (101325 Pa).

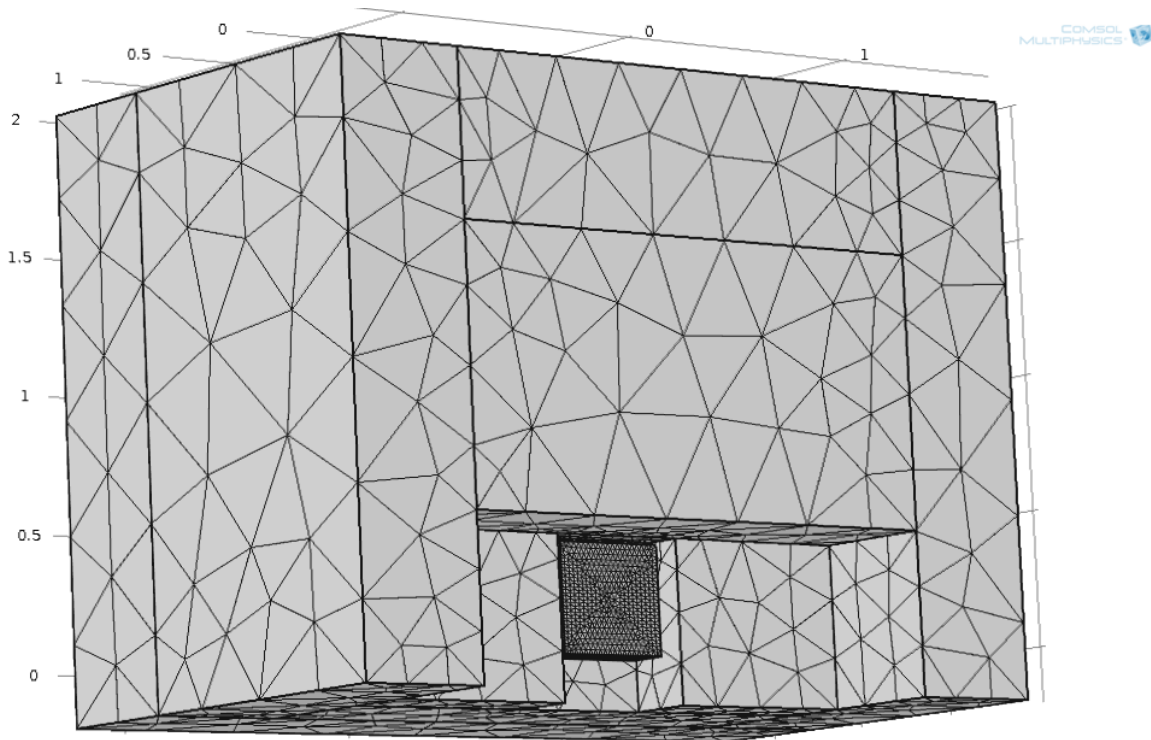


Fig [6]: Meshed COMSOL model with two PML slabs removed to reveal interior. The acoustic chamber is the densely meshed box, with the atmosphere being the box box directly on top. Everything else is PML slabs.

3.3 Acoustic mapping

3.3.1 General setup

The acoustic chamber is a box constructed from 16mm plywood, with two internal, moveable walls with speakers mounted inside. At various points there are holes drilled through the wall, where steel microphone holders have been mounted. The internal walls are held in place with 4 screws. Additionally, a lid was used in some experiments to try to improve the “quality” of the resonant modes, that is, decrease the drop in pressure when travelling along the z-axis. It covers the entire box, and is made from the same plywood, with a 2cm hole drilled every 11 centimetres along the middle. It is held in place by 8 screws.

Three different distances between the walls were tried, one at 858mm, one at 444mm one at 202mm. These were chosen for their predicted full wave resonance frequencies, i.e. frequencies of interest for the experiment. These were predicted to be around 400 hz, 800 hz, and 1700 hz, respectively. Slight deviations on the order of +/- 2mm may occur between

experiments due to the walls being fixed by hand (using calipers, measuring tape and a bubble level). A window was cut out in the box, and the wall was replaced by 16mm acrylic. The insides were painted black to reduce reflections from light sources. (Pictures are available in the appendix).

Mounted in each wall 10 cm above the bottom of the box are two Rondson TU100 driver units, their bandwidth listed as 150-10000 Hz.

For generating the signal a Wavetek 4MHz Function generator model 182a signal generator was used, set to produce sine waves.

A Tektronix TBS 1042 Oscilloscope was attached to the signal generator using a splitter, the other end feeding into the Crown CE1000 amplifier. The signal was then fed to the driver units using the same output channel (the cable being split).

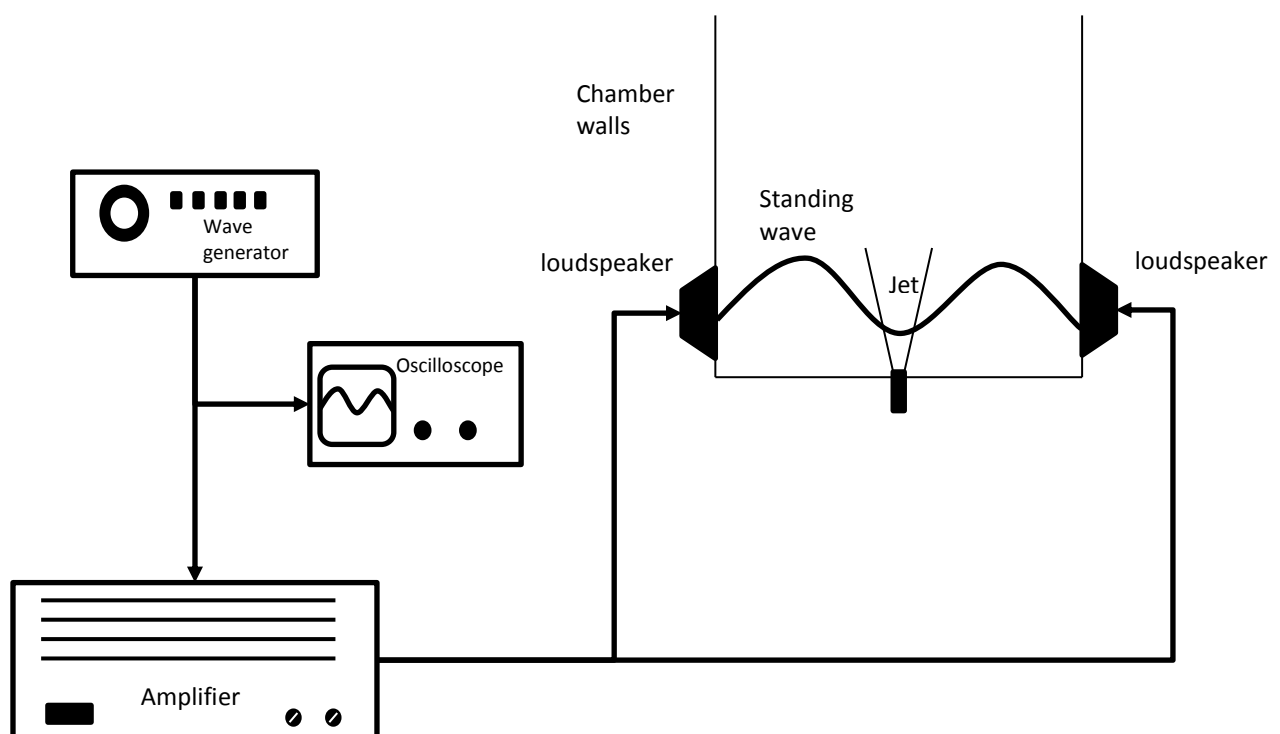


Fig [7]: Diagram showing the acoustic forcing setup

The microphones were 4 Bruel & Kjaer Pressure-field 1/4" Microphone type 4938, each connected to a separate microphone cable that fed into the Bruel & Kjaer type 2829 4 channel microphone power supply. The microphone power supply feeds three BNC cables, which were connected to the national instruments cDAQ-9174 with a NI9234 data acquisition (DAQ) module. The DAQ was connected to a windows computer running Labview 2013.

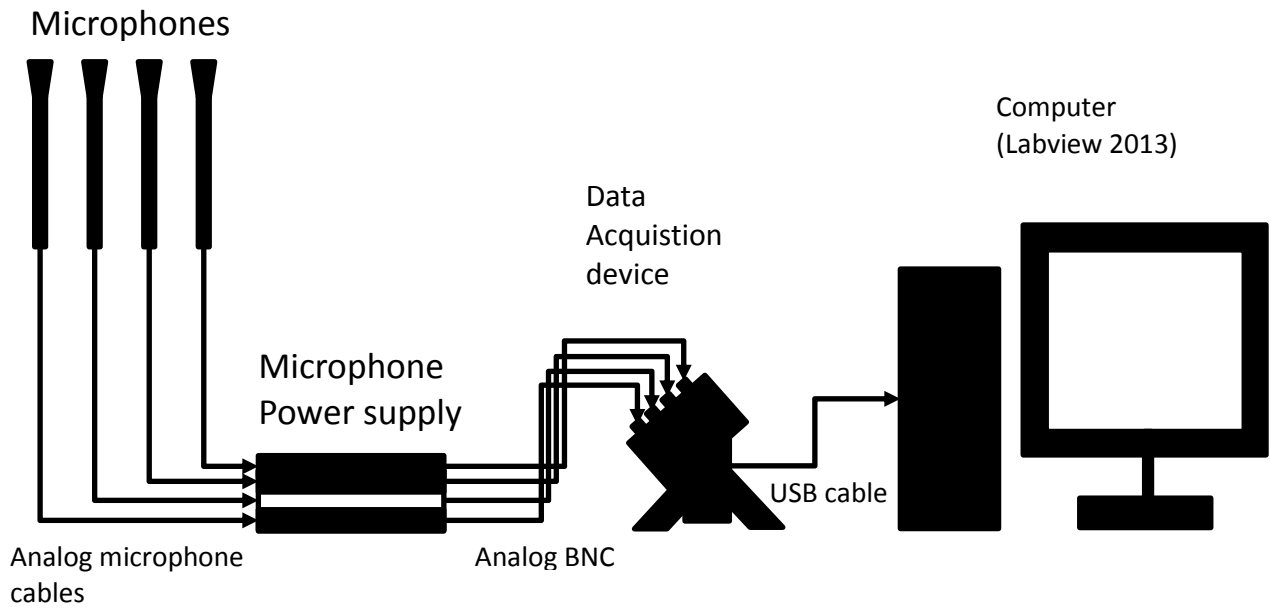


Fig [8]: Diagram showing the acoustic measurement setup

3.3.2 Microphone calibration

The mode shapes gained from the stated microphone ratios were somewhat unsatisfactory, so they were recalibrated against each other.

Using a single wall position at 858 mm, the microphones were cycled through the mid position and measurements were taken at 400, 1000 and 2000 Hz. Each microphone will then be measuring the same acoustic response. A reference microphone is chosen and other microphones have their response calibrated to that microphones response, using a least squares optimization procedure.

Microphone	Old ratio	New ratio
1	1.665 mV/Pa	1.527 mV/Pa
2	1.505 mV/Pa	1.504 mV/Pa
3	1.597 mV/Pa	1.695 mV/Pa
4	1.465 mV/Pa	1.465 mV/Pa

[Table 1: Old and new microphone responses]

3.3.3 Frequency Sweep and Mode shape

A frequency sweep or scan is testing the acoustic response at several different frequencies, processing it and presenting it against the frequency. The frequency sweeps give a good indication of the overall acoustic behaviour of the acoustic chamber. A strong acoustic response spike indicates that there is an eigenmode. However, it is necessary to have additional data before one can say anything meaningful about which modes appear in the box. This is where using multiple microphones comes into play; by doing so and plotting the

different signal RMS's against their corresponding locations in the chamber, one can compare this to theoretical mode shapes and thus determine which mode is present.

A total of 6 different frequency sweeps of the box were carried out, one for each configuration of the box: 858mm between the walls, 444mm between the walls, 202mm, and each once again with the lid. Four microphones placed at speaker axis height were used to measure the acoustic response over a frequency ranging from 300 Hz to 2000 Hz, at 10 Hz intervals. The configuration of these microphones differ from each box configuration, but they were generally chosen to give a picture of the response over half the box length. This was done due to the symmetric nature of the resonant mode; microphones placed over the full length of the box might give the same information with regards to the mode shape. Sweeps were conducted at 3 notches below 33 on the amplifier.

The voltage response of the microphones was recorded over 2 seconds for each frequency. The sample rate was 25600 Hz for most experiments; later experiments were done at 51200 Hz. The signal was then multiplied by a ratio corresponding to the voltage/pascal ratio. These signals were then fourier transformed, using matlab's in-built fast fourier transform (A form of DFT). The peak and location of the power of each of these transforms were then superimposed to give the frequency sweep graphs. In essence, this is finding the power spectral density (PSD) of the response at each frequency, and using the peaks from each PSD to form a new plot.

The mode shapes of the peaks in the resulting graphs were investigated using data from all four microphones. The RMS of the pressure from each microphone was taken, plotted, and then compared to modes found using COMSOL.

To gain additional information about the modes, microphone measurements were also conducted along the longitudinal axis at the resonant frequencies. A total of seven microphone positions were used, placed in the middle between the walls (with the exception of 202mm, where it was offset by 5 cm). Only four microphones were available at once, so the experiment would have to be repeated with different positions of the microphone. In order to verify that the RMS's measured correspond to each other in each repetition, one microphone was left in place between each experiment. As in previous experiments, the RMS was then taken and then compared to COMSOL simulations. Forcing and detailed mode shape investigation were conducted at 33 on the amplifier. The data is still useful to compare to data at other amplifier settings, as the mode shape is unaffected by forcing amplitude.

3.4 Jet

A mass flow controller (MFC) was connected to a seeder and an axisymmetric jet nozzle as shown in fig 9. For the experiments, the MFC was set to 70 SLPM (standard litres per minute). With a nozzle 1 cm diameter nozzle, this is equivalent to 14.9 m/s bulk velocity (from continuity). With kinematic viscosity ν assumed to be $15.68 \times 10^{-6} \text{ m}^2/\text{s}$, this gives $Re = \frac{DU_{bulk}}{\nu} = 9551$, similar to that presented in figures 3 and 4.

The image capture was set up for so called particle image velocimetry. A laser provides lighting for a camera in the form of a laser sheet, illuminating a cross section of the jet, visible because it has been seeded with particles. Two images are shot at a known, small, time interval (here: 10 microseconds), and image processing is used to calculate the particles displacement over that time interval, thus giving a vector field.

A custom seeder using a double laskin nozzle was used together with olive oil provide visible particles for the jet.

A Laser (Litron LDY300 PIV) and a high-speed camera Photron fastcam SA1.1 synchronized through DAVIS provided the image capture. For capture, the laser and camera were fired at 7200 Hz.

The high-speed camera had a 180mm lens attached, and was positioned 60 cm from the window in the box. The camera was calibrated before the measurements using the DAVIS dark image subtraction and background image subtraction, and a calibration plate on top of the jet nozzle, inside the box.

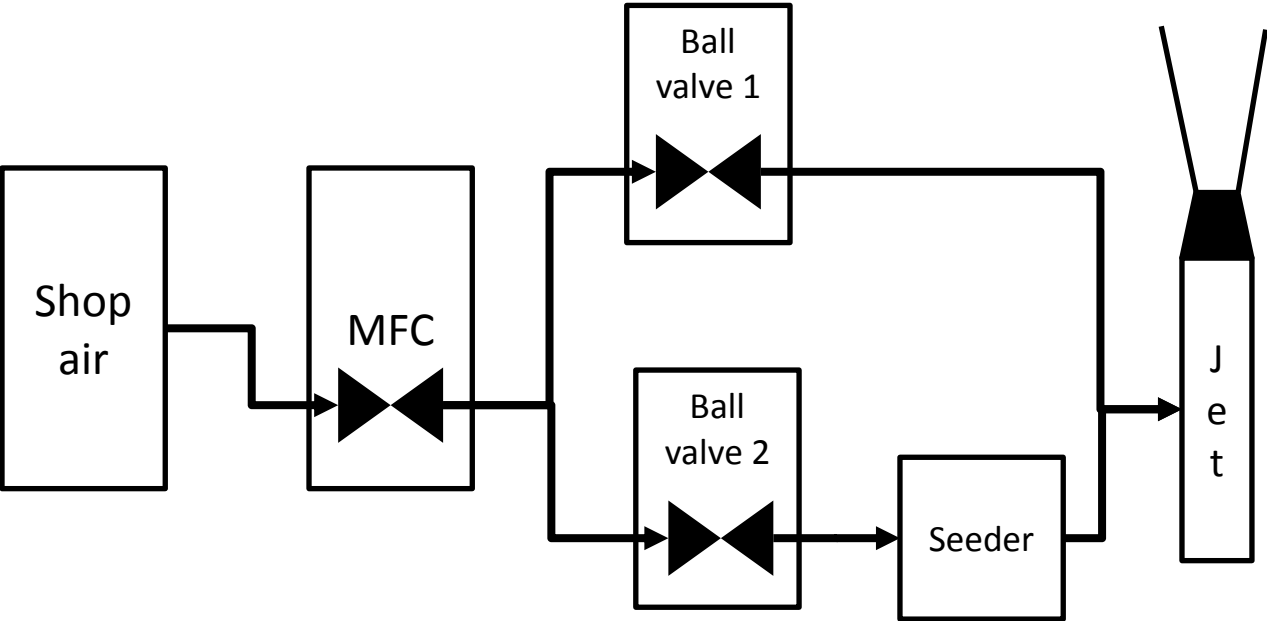


Fig [9]: Diagram showing the airflow/seeding setup

4 Results

4.1 Simulations

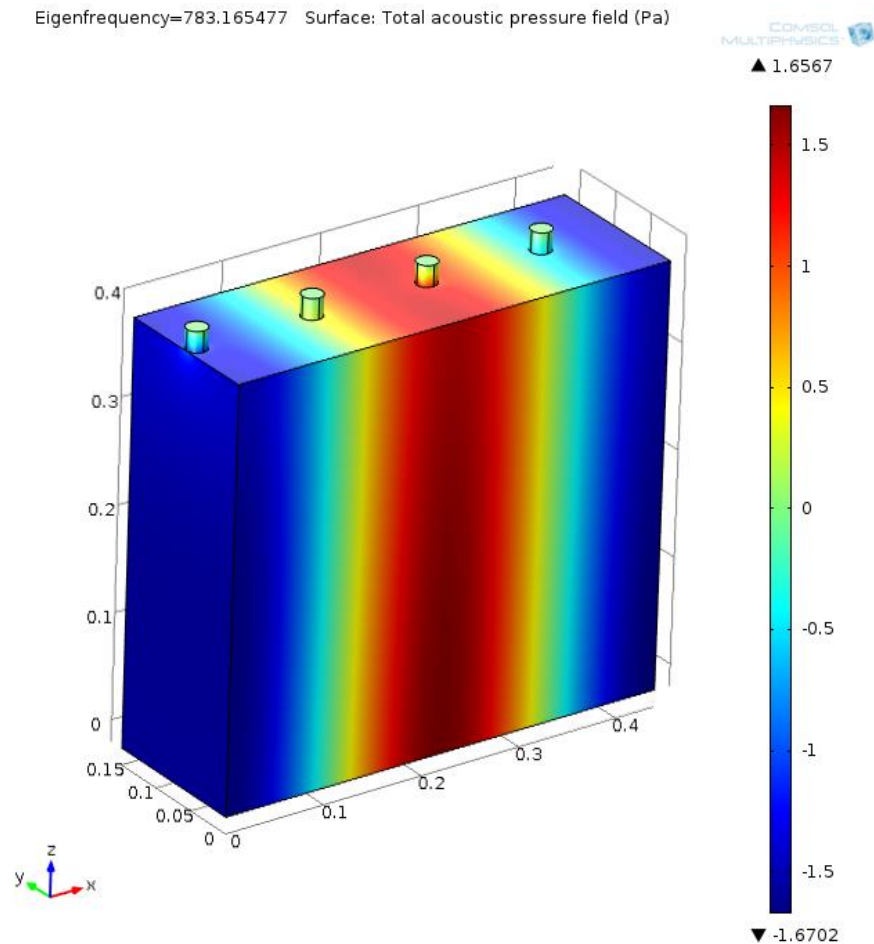


Fig [10]: COMSOL 3d surface plot of the acoustic field in a 444mm long chamber with a lid

Above (Fig. 10) is an example of a result of a COMSOL simulation. Displayed is a colour plot of the interior of the box, the “pegs” on the top being the holes in the lid. The colouring indicates acoustic pressure (i.e. deviation from atmospheric pressure) at the instant of maximum amplitude. The mode shown is the 2,0,0 mode of the box at 444mm. Below (Fig. 11) is the same simulation without the lid.

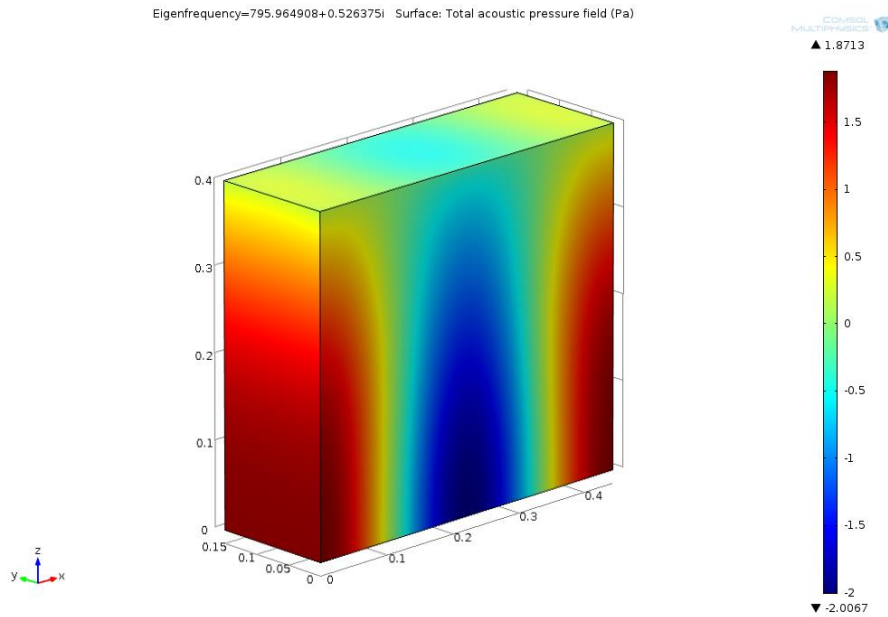


Fig [11]: COMSOL 3d surface plot of the acoustic field in a 444mm long chamber without a lid

The most notable difference is the gradient in pressure towards the top of the box. This stems from the open boundary where pressure the acoustic pressure is zero, and as such a gradient must form lest there be a discontinuity. The open end also means that the pressure isn't going to be uniform at the top of the chamber; the acoustic field will extend into the surrounding space. Below (fig 12.) is an isosurface plot where the box and surrounding atmosphere is represented by a wireframe. It is immediately clear how the acoustic field bulges into the atmosphere.

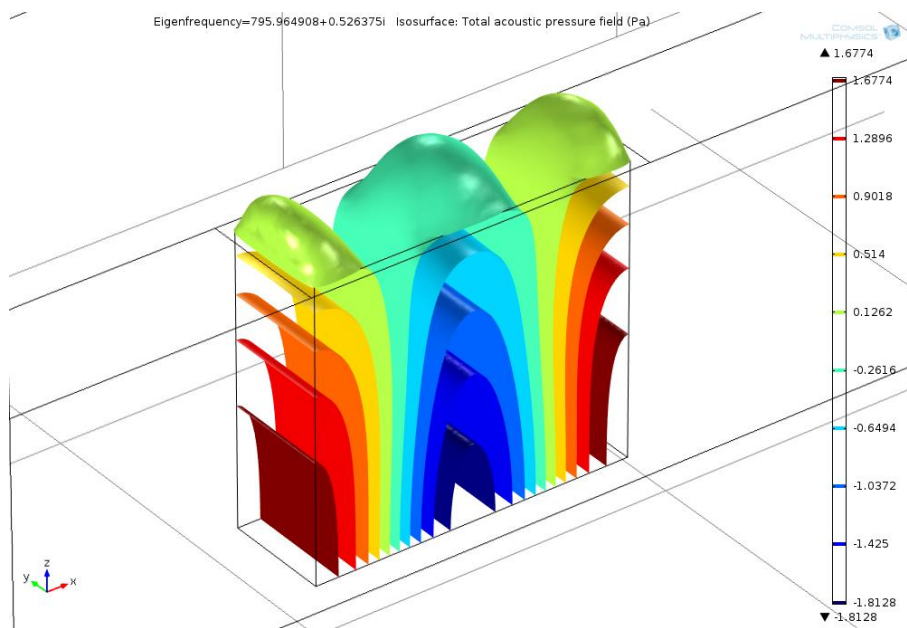
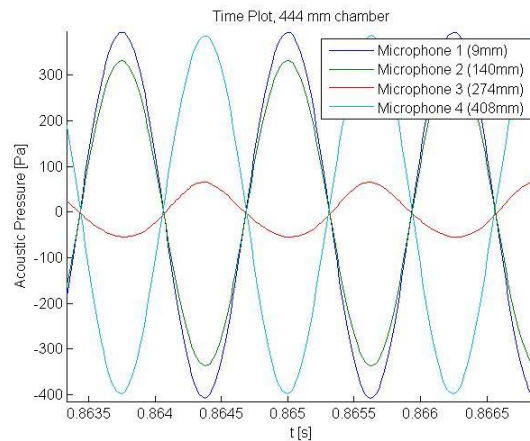


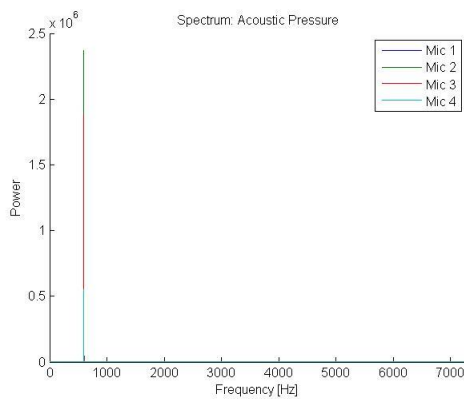
Fig [12]: COMSOL 3d isosurface plot of the acoustic field in a 444mm long chamber without a lid

4.2 Frequency sweeps

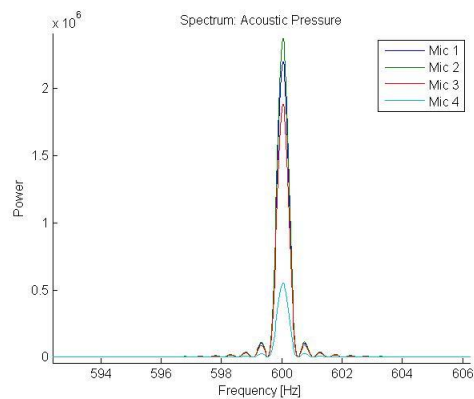
Below is an example of a small excerpt from a typical microphone signal. The waves are typically sinusoidal, and may be in varying degrees of phase with each other.



[Fig [13]: Example of microphone data plotted against time. This is a sample from 800 Hz forcing, without a lid



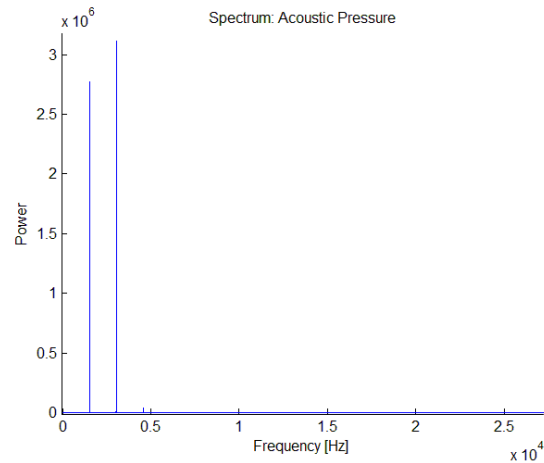
[Fig 13a]: PSD of a sample taken at 600 Hz forcing, 444mm long chamber without a lid



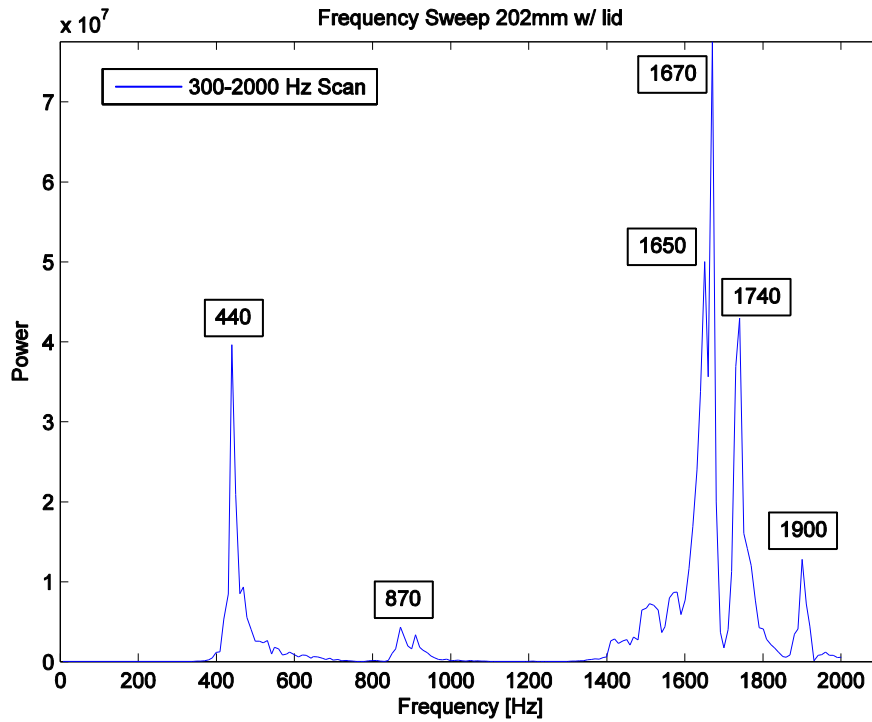
[Fig 13b]: PSD of a sample taken at 600 Hz forcing, 444mm long chamber without a lid, zoomed around the

Fig 13a and 13b show typical PSDs of a microphone data sample. Usually there is one large visible spike; any other spikes are usually at least two orders of magnitude below, and are thus negligible. However, there may be cases where there are multiple prominent spikes, as seen in Fig. 14. Here, there are 3 spikes visible, one at 1520 Hz, one at 3040 Hz, and finally one barely visible at 4560 (note that they are multiples). The largest response here is actually not the frequency it was forced at (1520 Hz), but its double, 3040 Hz. Responses where another

frequency than the forcing frequency is significant occurs only in low power responses. They appear to be practically zero in the frequency sweeps, being two or more orders of magnitude lower. The frequency sweeps have thus been modified, such that the response at some frequencies is not the largest spike at PSD, but the spike that lies within 5 Hz of the forcing frequency.



[Fig 14]: PSD of a sample taken at 1520 Hz forcing, 858mm long chamber without a lid



[Fig 15]: Frequency sweep of the 202mm long chamber with lid

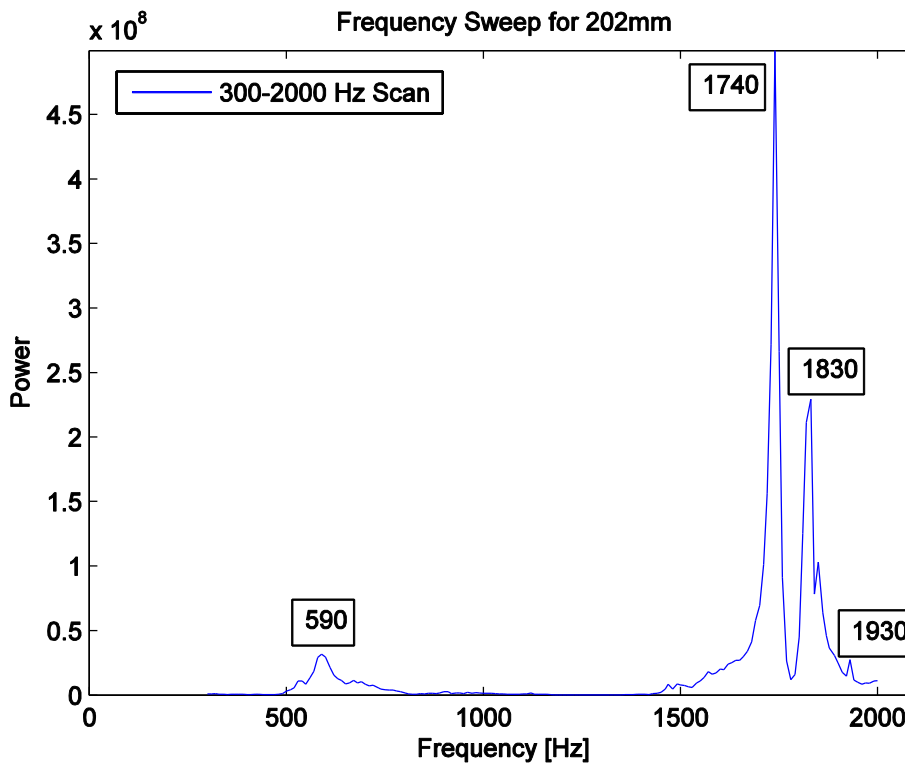


[Fig 16]: Frequency sweep of the 202mm long chamber without the lid

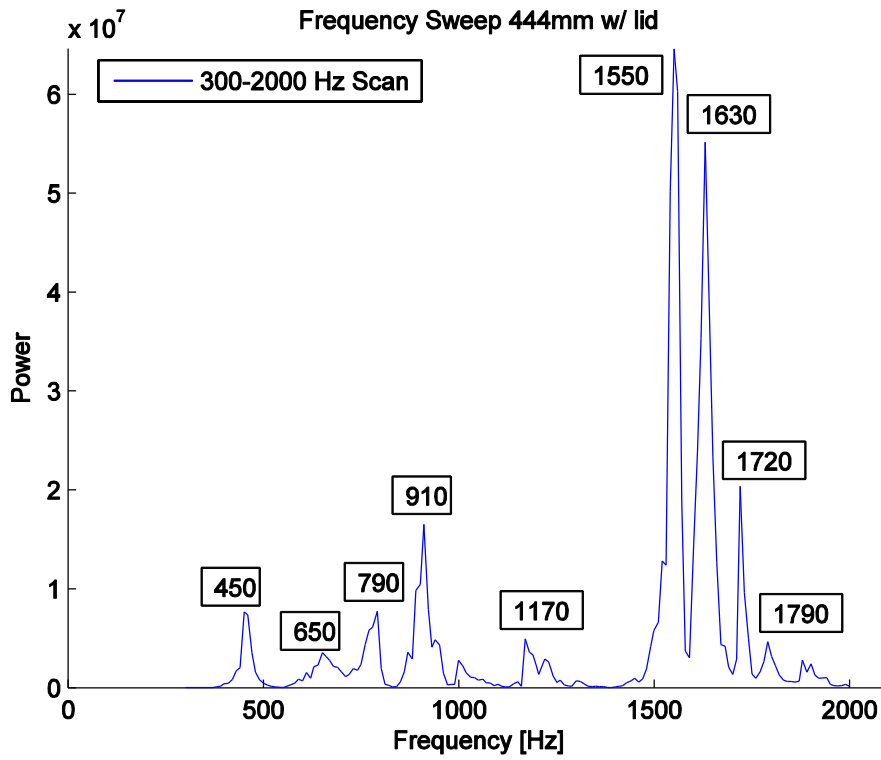


[Fig 17]: Frequency sweep of the 444mm long chamber without the lid

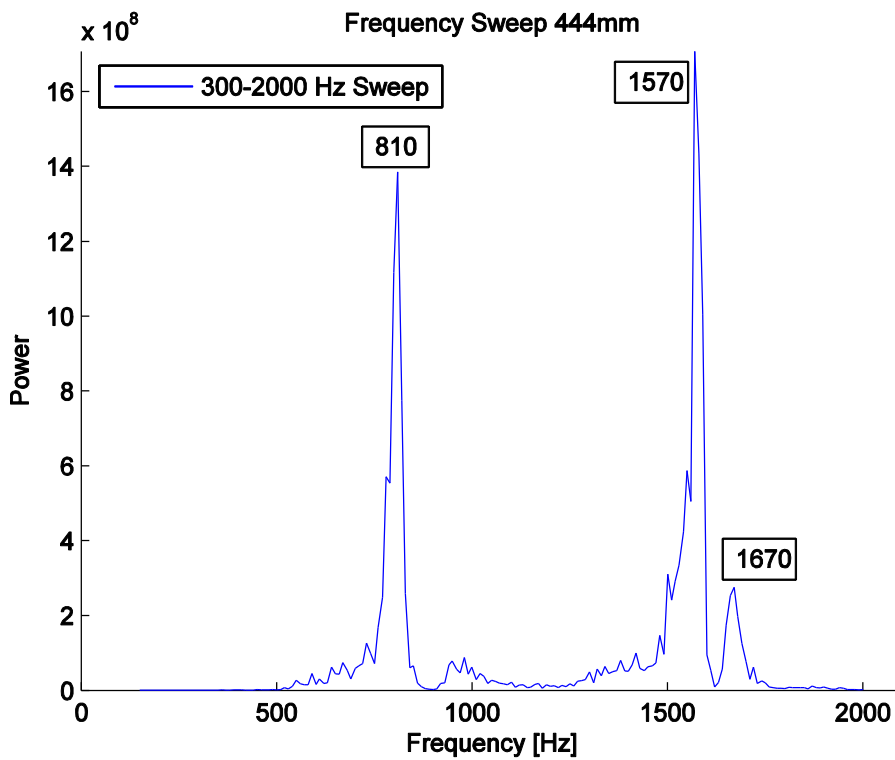


[Fig 18]: Frequency sweep of the 444mm long chamber without the lid

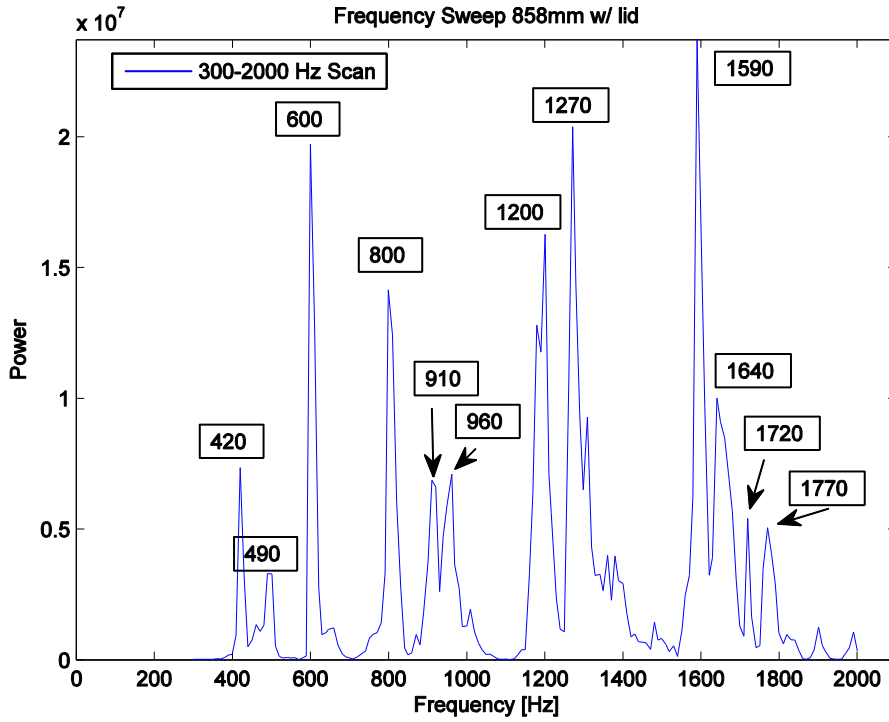


[Fig 19]: Frequency sweep of the 858mm long chamber without the lid

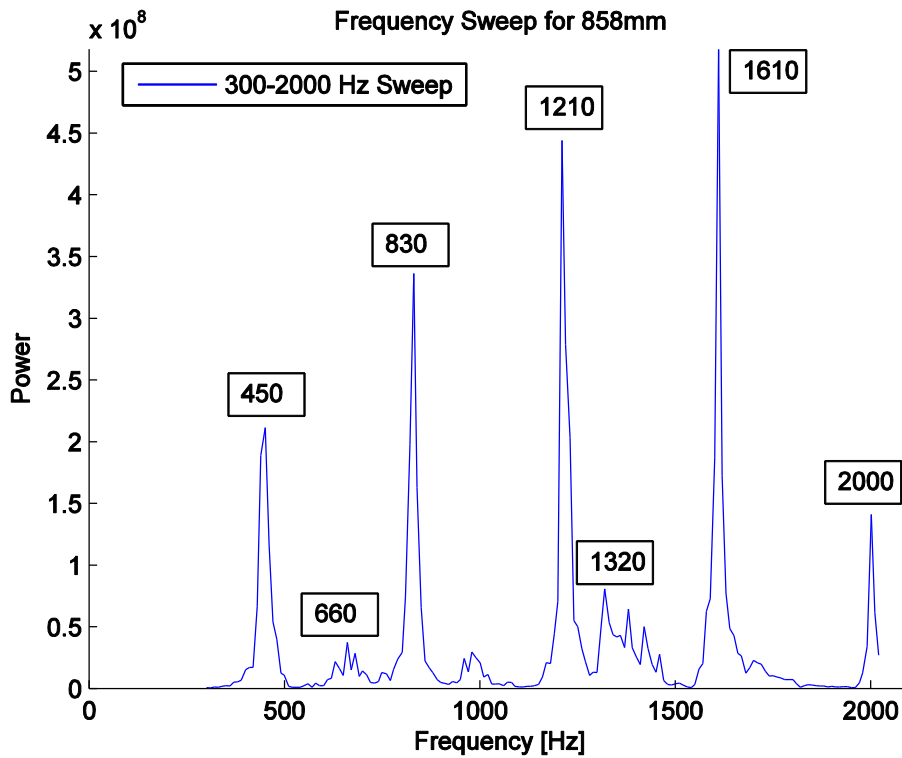


[Fig 20]: Frequency sweep of the 858mm long chamber without the lid

4.3 Mode locations and shapes

In order to identify an eigenmode, a spike in the frequency sweep is checked against the microphone RMSs as shown in figure 18, together with the theoretical wave amplitude shape, and COMSOL data where necessary.

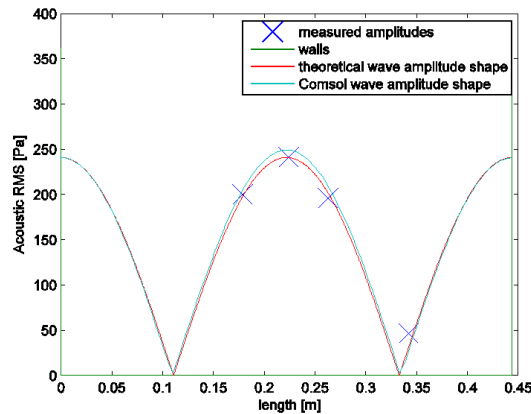


[Fig 18]: Microphone amplitudes of the 444mm chamber, at 810 Hz. Example of how modes are identified

Below are frequencies of the modes found by COMSOL and the frequency of the observed modes of the experiment. The identification has been limited to axial and quasi-axial modes only, as more complex modes are not desired and requires more measurements in general to correctly identify. They are also in general weaker than axial modes, and thus less likely to appear in the sweep.

202mm length modes					
With lid			Without lid		
Mode Number (X,Y,Z)	COMSOL	Experiment	Mode Number (X,Y,Z)	COMSOL	Experiment
Helmholtz mode	69 Hz	Out of scan range	0,0,1	214 Hz	Out of scan range
0,0,1	440 Hz	440	0,0,2	643 Hz	Not observed
1,0,0	854 Hz	Not observed	1,0,1	877 Hz	Not observed
0,0,2	864 Hz	870	0,0,3	1072 Hz	Not observed
0,1,0	1144 Hz	Not Observed	0,1,1	1163 Hz	Not observed
0,0,3	1291 Hz	Not Observed	0,0,4	1501 Hz	Not observed
2,0,0	1703 Hz	1670	2,0,1	1715 Hz	1740
0,0,4	1719 Hz	Not observed	0,0,5	1931 Hz	Not observed

[Table 2]: Modes of the 202mm long chamber

444mm length modes					
With lid			Without lid		
Mode Number (X,Y,Z)	COMSOL	Experiment	Mode Number (X,Y,Z)	COMSOL	Experiment
Helmholtz mode	69 Hz	Out of scan range	0,0,1	214 Hz	Out of scan range
1,0,0	396 Hz	Not observed	1,0,1	442 Hz	Not observed
0,0,1	440 Hz	450	0,0,2	643 Hz	Not observed
2,0,0	783 Hz	780	2,0,1	802 Hz	810
0,0,2	864 Hz	Not observed	0,0,3	1071 Hz	Not observed
0,1,0	1144 Hz	Not observed	0,1,1	1164 Hz	Not observed
3,0,0	1172 Hz	Not observed	3,0,1	1179 Hz	Not observed
0,0,3	1290 Hz	Not observed	0,0,4	1501 Hz	Not observed
4,0,0	1562 Hz	1550	4,0,1	1561 Hz	1570
			0,0,5	1931 Hz	Not observed
5,0,0	1951 Hz	Not observed	5,0,1	1944 Hz	Not observed

[Table 3]: Modes of the 444mm long chamber

858mm length modes					
With lid			Without lid		
Mode Number (X,Y,Z)	COMSOL	Experiment	Mode Number (X,Y,Z)	COMSOL	Experiment
Helmholtz mode	70 Hz	Out of scan range	0,0,1	214 Hz	Out of scan range
1,0,0	213 Hz	Out of scan range	1,0,1	293 Hz	Not observed
2,0,0	406 Hz	420 Hz	2,0,1	454 Hz	450
0,0,1	441 Hz	Not observed	3,0,1	637 Hz	Not observed
3,0,0	604 Hz	Not observed*	0,0,2	643 Hz	Not observed
4,0,0	803 Hz	800 Hz	4,0,1	828 Hz	830
0,0,2	863 Hz	Not observed	5,0,1	1023 Hz	Not observed
5,0,0	1003 Hz	Not observed	0,0,3	1072 Hz	Not observed
0,1,0	1144 Hz	Not observed	0,1,1	1164 Hz	Not observed
6,0,0	1202 Hz	1200 Hz (dist)	6,0,1	1219 Hz	1210
0,0,3	1290 Hz	1270(dist)	7,0,1	1416 Hz	Not observed
7,0,0	1402 Hz	Not observed	0,0,4	1501 Hz	Not observed
8,0,0	1601 Hz	1600 Hz	8,0,1	1614 Hz	1610 (distorted)
0,0,4	1718 Hz	1720(dist)	9,0,1	1812 Hz	Not observed
9,0,0	1801 Hz	Not observed	0,0,5	1931 Hz	Not observed
10,0,0	2001 Hz	1990 Hz (dist)	10,0,1	2010 Hz	2000

[Table 4]: Modes of the 858mm long chamber. (dist) means the mode is likely present, but is distorted

Most modes that are found with COMSOL do not appear in the experiment. For example, it is worth noting that the x-axis modes are the strongest modes present in most cases, however, no odd-numbered x-axis modes appear. This is likely caused by the speakers running in phase rather than out of phase. When two speakers are running in phase, and at an odd-numbered x-mode, they will try to excite opposite acoustic fields, causing them to cancel each other. To verify this, the speakers were run out of phase in the 444mm lidless chamber configuration, but otherwise following the frequency sweep procedure. The sweep was conducted over just 420-440 Hz, but this was sufficient to identify the missing (1,0,1) mode (Figs 21a-b).

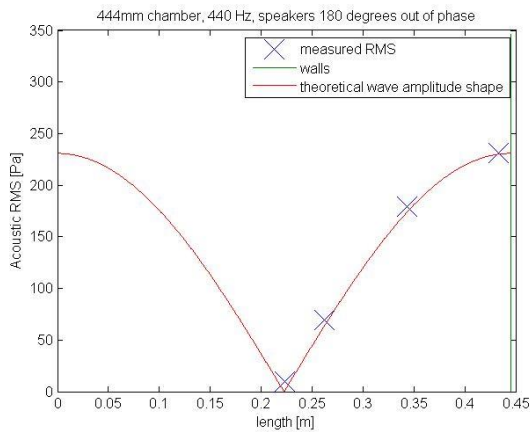


[Fig 21a]: Microphone amplitudes of the 444mm chamber, at 440 Hz, 180 degrees out of phase

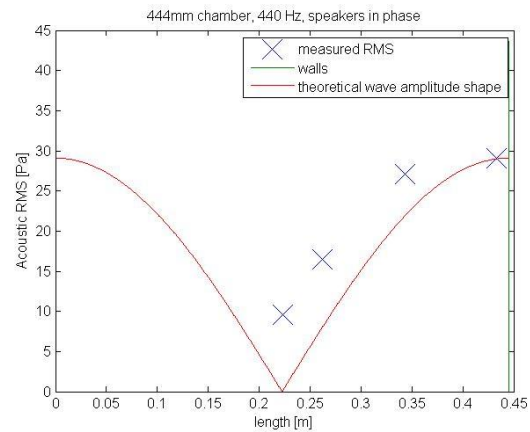


[Fig 21b]: Microphone amplitudes of the 444mm chamber, at 440 Hz, in phase

Arguably, the (1,0,1) mode has a certain presence even when being run in phase. It is however both weak and distorted. The antinode is a minimum that's on the same order as the maximum, and the general impression is that the mode shape has been “flattened”.

For other modes that are not found, modes that are present in theory are simply too weak to be observed in the box, as they are drowned in other modes. One such case is the z-axis modes in any of the lidless sweeps.

A third possibility is that a close mode may distort an otherwise present mode. As the frequency increases, so too does the density of (theoretical) modes. If a mode's frequency is close to another's they may interfere with each other.

It is apparent that the dynamics of the box are greatly altered by the lid. Without it, the sweep turns out relatively clean with few to no modes of note in between the desired x-modes. With the lid, several other modes become prominent and appear. Naturally, the z-axial modes become stronger, and so appear in the tables. This doesn't account for all spikes in the sweeps however; the rest are likely from complex modes, due to the strengthened z-axis acoustics together with the dominant x-axis.

An example would be the spike at 1630 Hz with the 444mm acoustic chamber with lid, where the excited mode is likely the 4,0,1 mode, as demonstrated by the Figs 22a-22b.

Eigenfrequency=1621.921645 Surface: Total acoustic pressure field (Pa)

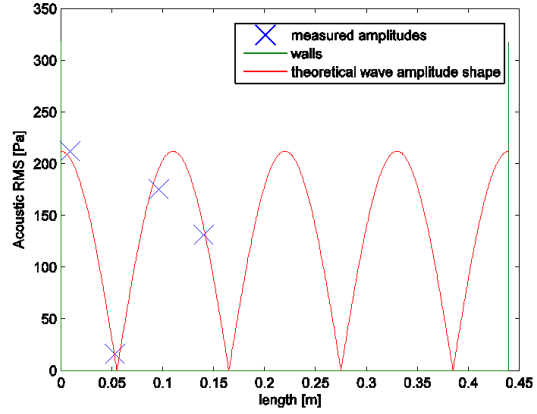
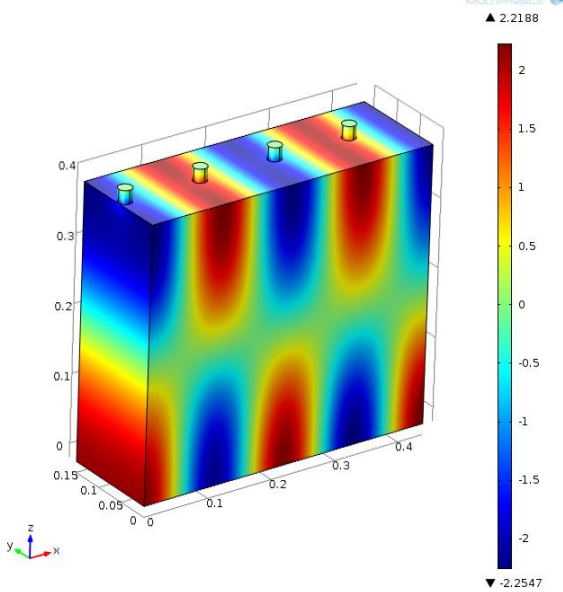


[Fig 22a]: Comsol simulation of 4,0,1 mode in 444mm long chamber, with lid

[Fig 22b]: Microphone amplitudes of the 444mm chamber, at 1620 Hz, with lid

The location of the first mode agrees reasonably well even with simple theory, as given in eq. 15 (lid) and 16 (lidless). The inverse relationship between frequency as chamber length is readily apparent in figure 21.

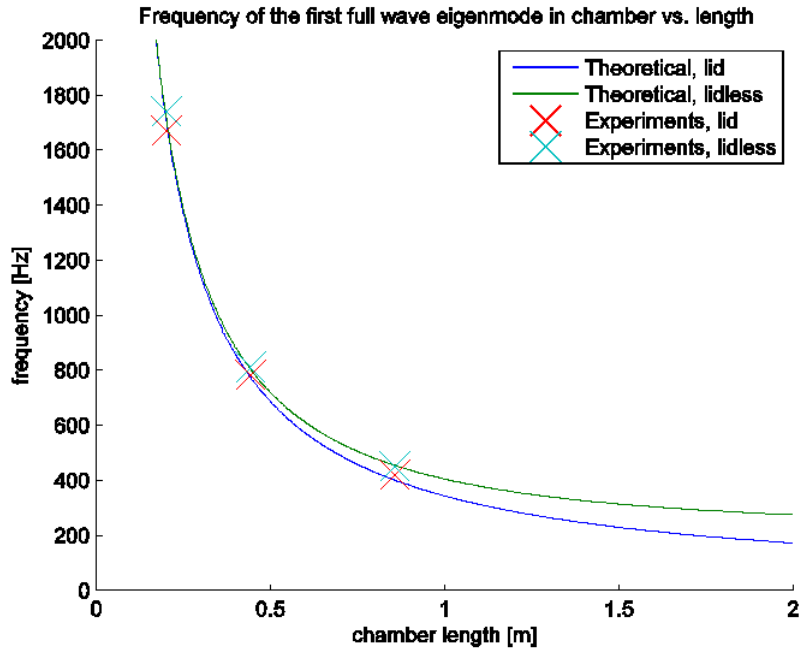


[Fig 23]: Relationship between the frequency of the first full wave resonant mode and the length of the chamber

Somewhat unexpectedly, the strength of the first full wave mode in the box is consistently weaker with the lid. A possible explanation is the holes in the lid. Though they are necessary to let air out if a jet flow is to be run through the chamber, they present a boundary of alternating pressure conditions. Though a fully enclosed chamber might have stronger modes, it appears that a compromise with holes is unviable, at least in terms of mode strength.

The strength of each mode also decreases with length. This might be due to both having an open boundary at the top that grows larger with the chamber length. It might also be simply due to the increased size leading to increased attenuation as the waves have to travel further. It is also likely that the response of the speakers affect the result.

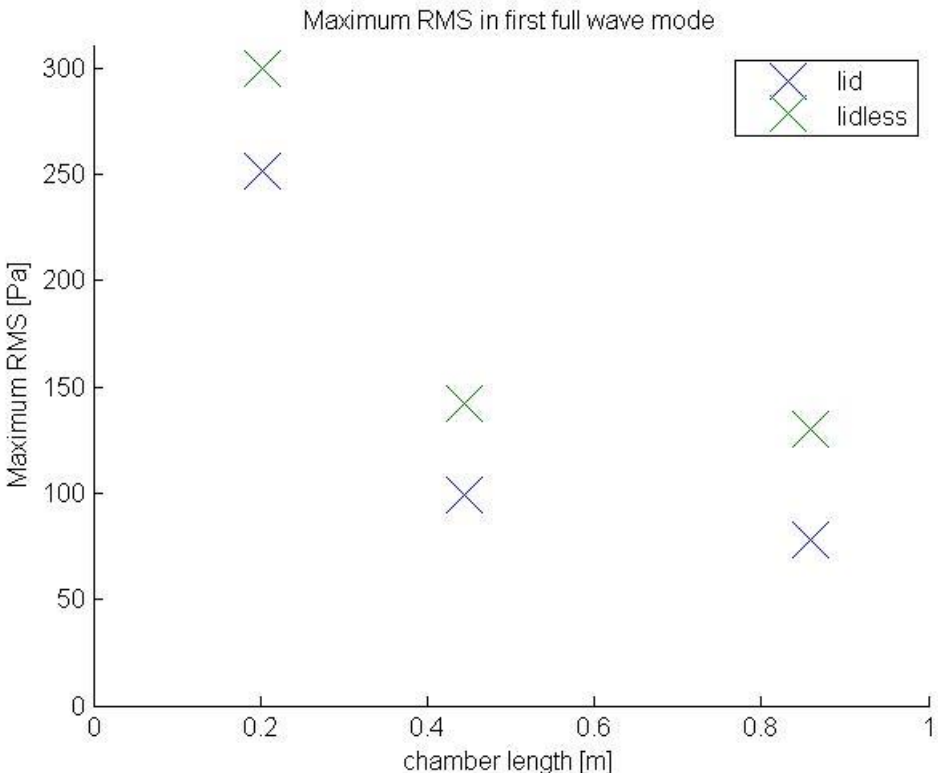


[Fig 24]: Maximum acoustic RMS found in microphone at wall during frequency sweeps.

The mode shapes with and without the lid are quite different from one another, as seen in these examples. While the lid-mode is nearly flat in the z-direction, the lidless mode tapers off in an approximate quarter sine-wave, compare figures 10-12 of the 3d COMSOL rendering. As each study was repeated, it turned out that despite best efforts to control all variables a pressure difference between the first and the second trial would arise in some cases. Examples of this is given Figs 25a-b.

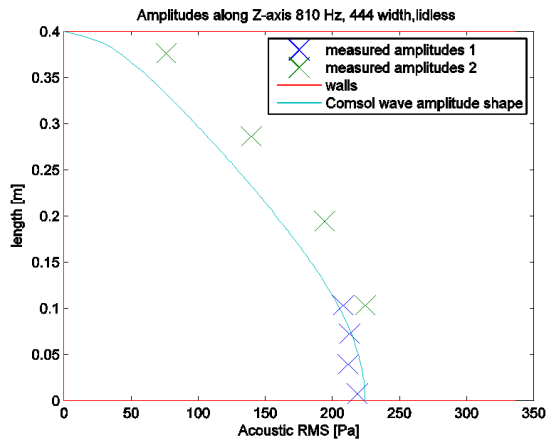


[Fig 25a]: Z-axis mode investigation, 444 length, lidless, 810 Hz. Example of difference between first experiment and

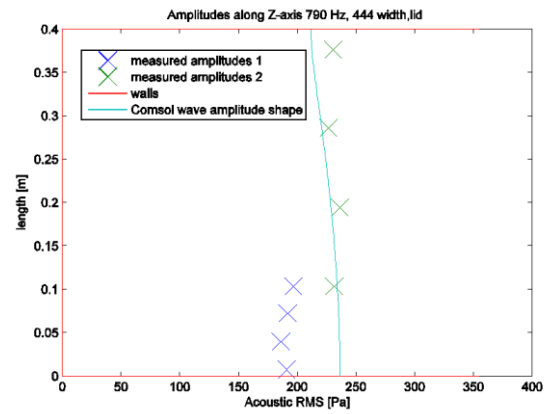


[Fig 25b]: Z-axis mode investigation, 444 length, lid, 790 Hz. Example of difference between first experiment and

Though this points out that measurements be taken with a proverbial grain of salt, the purpose was to find the overall mode shape, and not the specific amplitudes at different points. Thus in the following figures, the one of the two measurement runs had the measured difference between the microphone that wasn't moved added to it in order to better compare with the mode shape. In order to not present false data, the measured RMSs have also been normalised by their maximum. It was taken care that the frequencies not deviate with more than 1 Hz, so the modes should be more or less the same. The original figures, complete with minor or more significant discrepancies, can be found in the appendix.

Another discrepancy was that for the mini-sweeps carried out to find the resonant modes, the strongest mode was found 10 Hz over from the full sweep counterparts (1680 Hz vs 1670 Hz, and 800 Hz vs 810 Hz). This is likely due to the walls being slightly closer/further away (as noted in chap 3.3.1), or not completely straight.

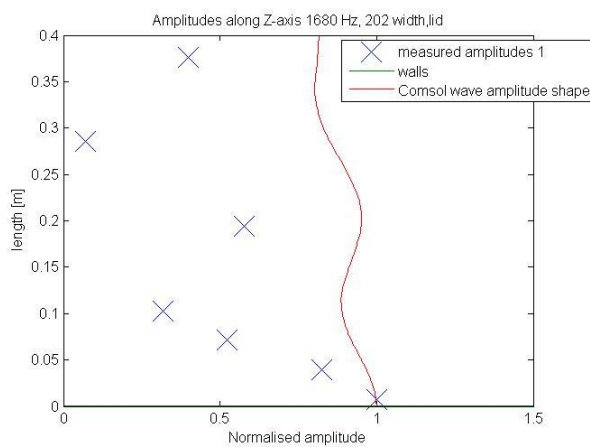


[Fig 26a]: Z-axis mode investigation, 202 mm length, lid, 1680 Hz.

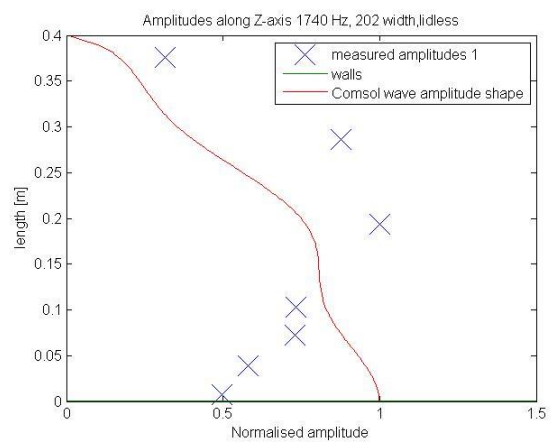


[Fig 26b]: Z-axis mode investigation, 202 mm length, lidless, 1740 Hz.

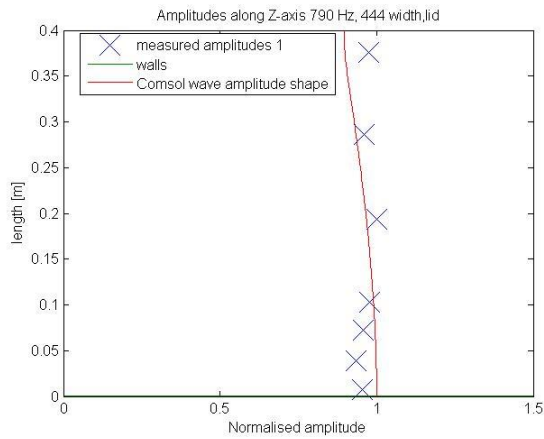


[Fig 27a]: Z-axis mode investigation, 444mm length, lid, 790 Hz.

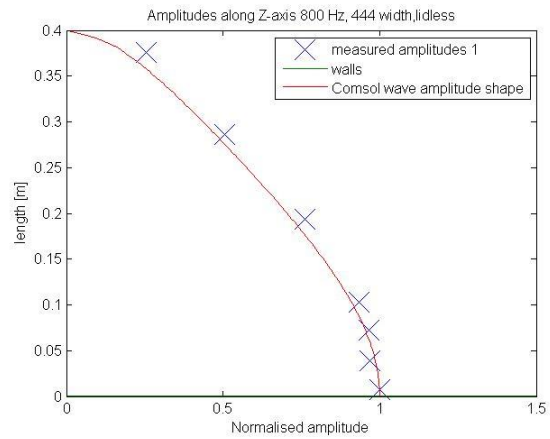


[Fig 27b]: Z-axis mode investigation, 444 mm length, lidless, 800 Hz.

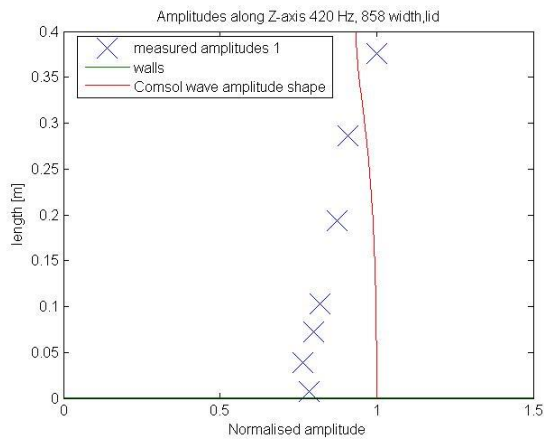


[Fig 28a]: Z-axis mode investigation, 858 mm length, lid, 420 Hz.

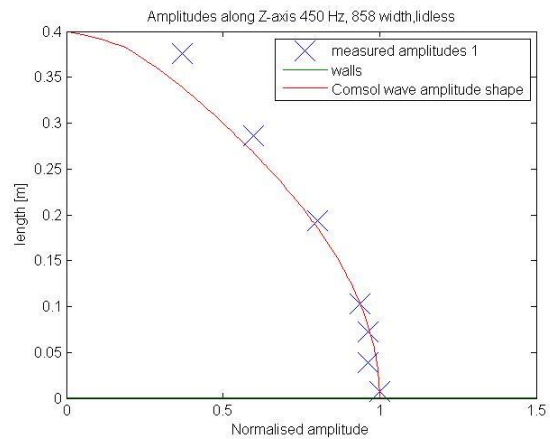


[Fig 28b]: Z-axis mode investigation, 858 mm length, lid, 450 Hz.

From fig. 26a-b it is apparent that both with and without the lid, the modes at 202 length are heavily distorted compared to the COMSOL simulation. With the lid, it looks almost as if it is a full wave along the z-axis, while the lidless doesn't form its maximum at the wall, as one would expect. The simulated COMSOL mode is also a far cry from the expected quarter sinusoid, which is further evidence of the distortion of the mode. It appears that the walls being mounted that close, the length being half the height and close to the width means that the length no longer holds the dominant mode activity, and is therefore unsuitable for jet forcing.

From figure 27a-b, 444mm looks much more promising. Both with the lid and without, the data follows the COMSOL simulations quite closely. COMSOL underestimates the outer points slightly in the lidless simulation. With the lid, there's a slight bend to the curve which is reminiscent of a very mild distortion similar to that in fig 26a.

For figure 28a, the resulting pressure distribution is unexpected, and looks almost as though it has been reversed compared to the COMSOL simulation. It might be that the mode is

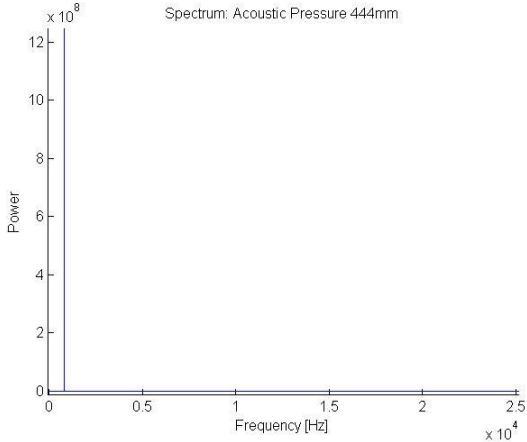
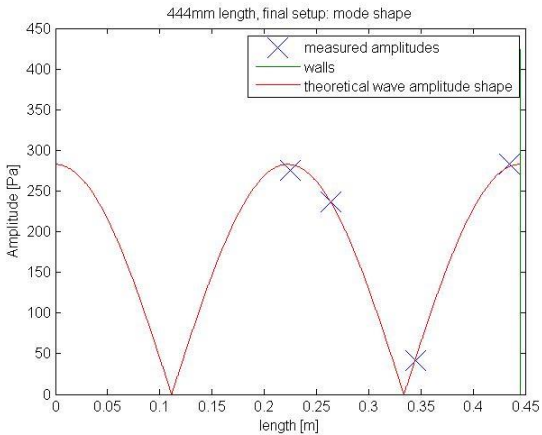
distorted; since it is the weakest mode of the 6 it is more prone to it. 28b looks much like 27b, though with a slightly higher pressure than predicted toward the top. This might be caused by mesh coarseness in COMSOL, such that it underestimates how much the acoustic field enters the surrounding atmosphere.

Based on these plots and prior plots and tables, the 444mm lidless was chosen as the configuration for forcing the jet. The mode is the cleanest of all 6, and is stronger than its lid counterpart, though not in terms of pressure conservation along the z-axis. The frequency sweeps also indicate that the lid is less reliable; there are many more spikes than without the lid. However, with these flaws quantified and accounted for, one could use the lid for forcing the jet.

In terms of the fluid dynamics recirculation might have been a problem with the lid. Though earlier project work [12] determined that the lid would have sufficient exhaust ports for the jet to be treated as free at 10 m/s bulk velocity, the seeder turned out to require 15 m/s in order to function properly. The advantage offered by the lid was thus offset by additional studies required in order to verify its suitability.

As the camera system was not capable of running at multiples of 810 (other than 10), 800 was chosen as the forcing frequency instead, the difference in mode shape being negligible and a pressure loss of around 20%. The fact that the mode was found at 800 Hz (fig 25b) in some cases indicates that the mode is between 810 and 800.

A mode shape measurement was taken at forcing conditions, and repeated with flow.



<p>[Fig 29a]: Mode shape, without flow</p>	<p>[Fig 29a]: Spectrum, without flow. Single spike at 800 Hz.</p>
---	--

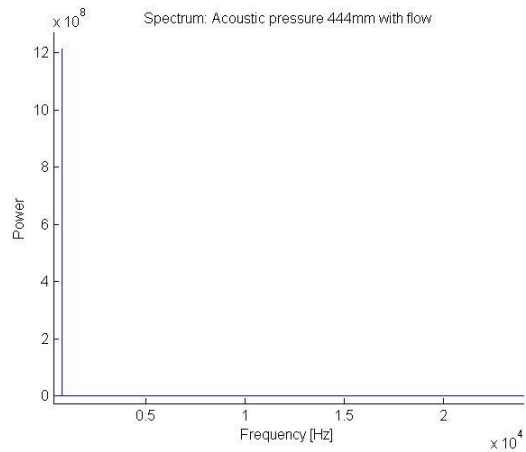
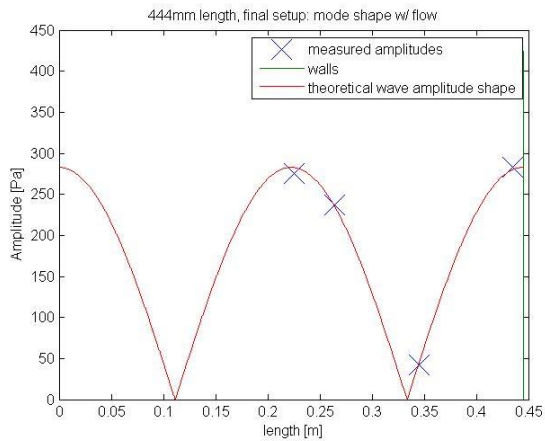


[Fig 30a]: Mode shape, with flow	[Fig 30a]: Spectrum, with flow. Single spike at 800 Hz.
---	--

4.4 Forced Jet

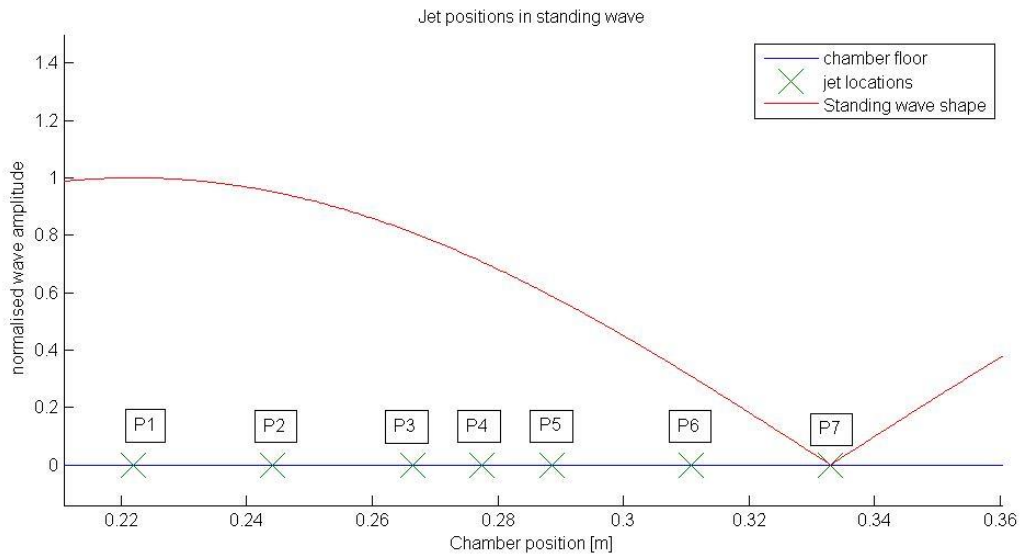


[Fig 31]: Jet positions in chamber

There are 7 total positions for the jet, starting at the antinode position P_1 (222mm from each wall) and moving toward the node in increments equal to $\left(\frac{L}{4}\right)\frac{1}{5}$, where L is the distance between the walls. $\frac{L}{4}$ is also the distance between the node position P_7 and the antinode position P_1 . The seventh position is in the middle between the node and antinode. The

antinode is on the right side of the jet, while the node is on the left. All positions are shown in figure 31.

As the framerate of the capture was set to 7200 Hz, every 9 frames will describe a period T of forcing. The top and bottom of the images are slightly out of focus, and this is due to a bar holding the Perspex in place making it necessary to angle the camera down. The vortices break up faster on the right side than the left, and this is likely due to the jet nozzle being slightly bent out of shape.

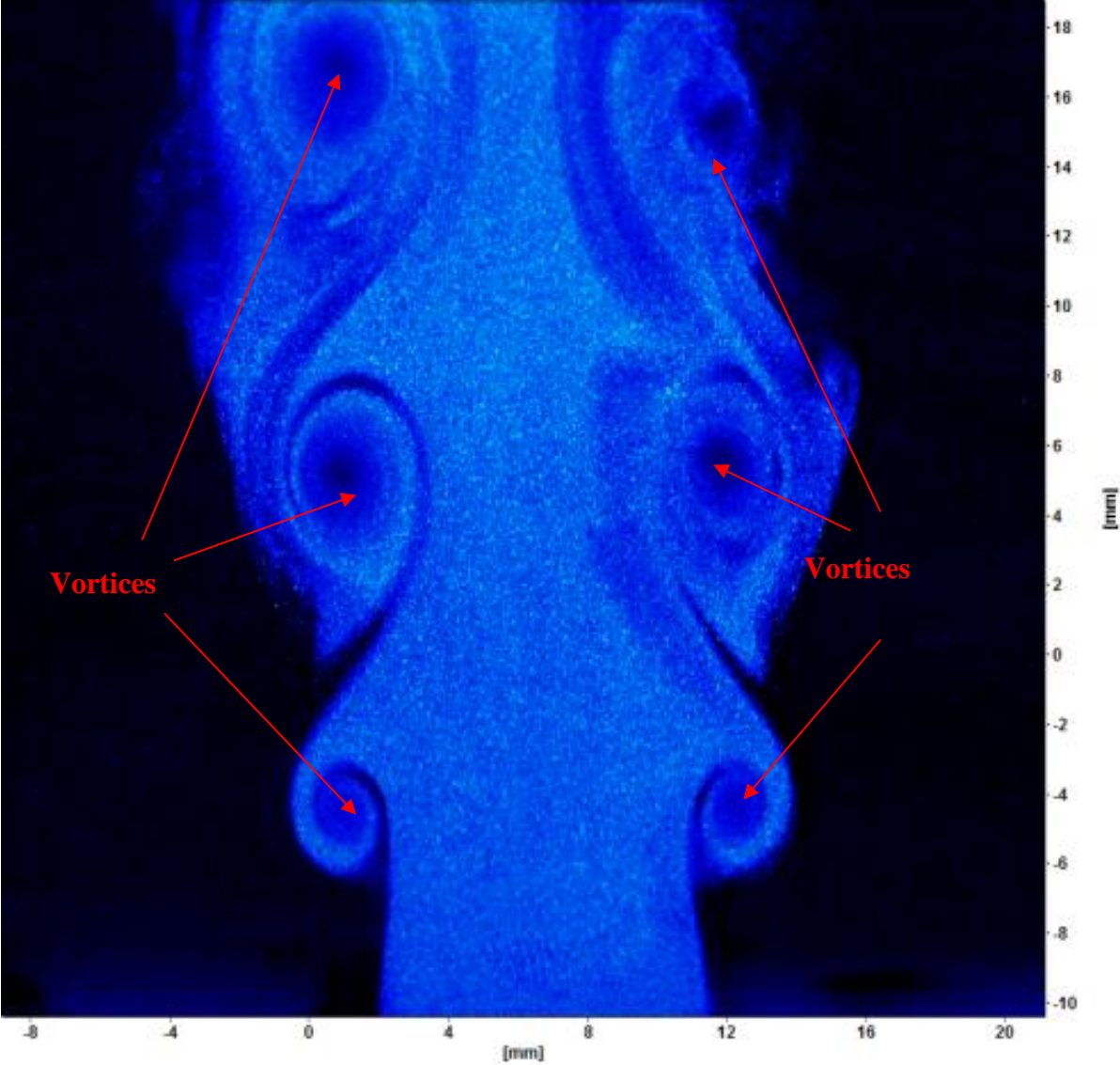


[Fig 32] Example full size image of forced jet, same images as in 34a

Unforced

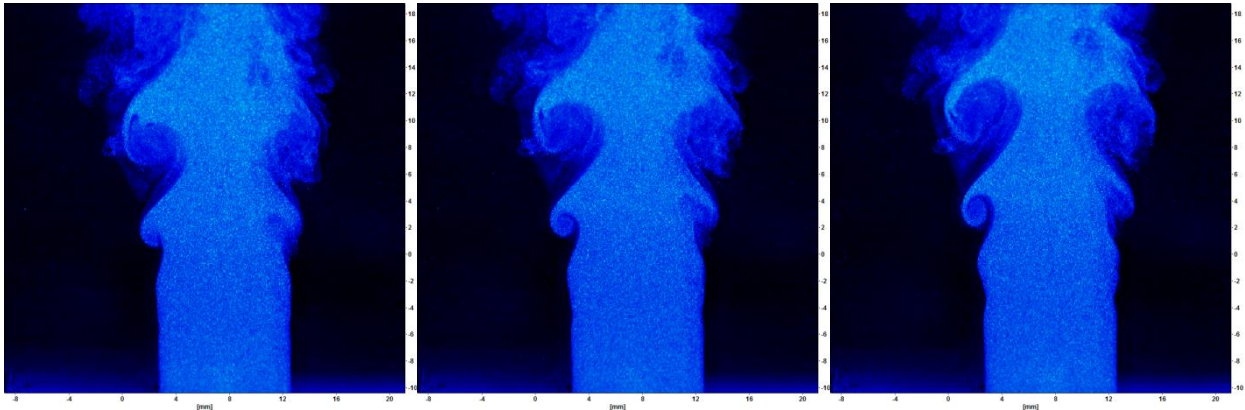


[Fig 33a]

[Fig 33b]

[fig 33c]

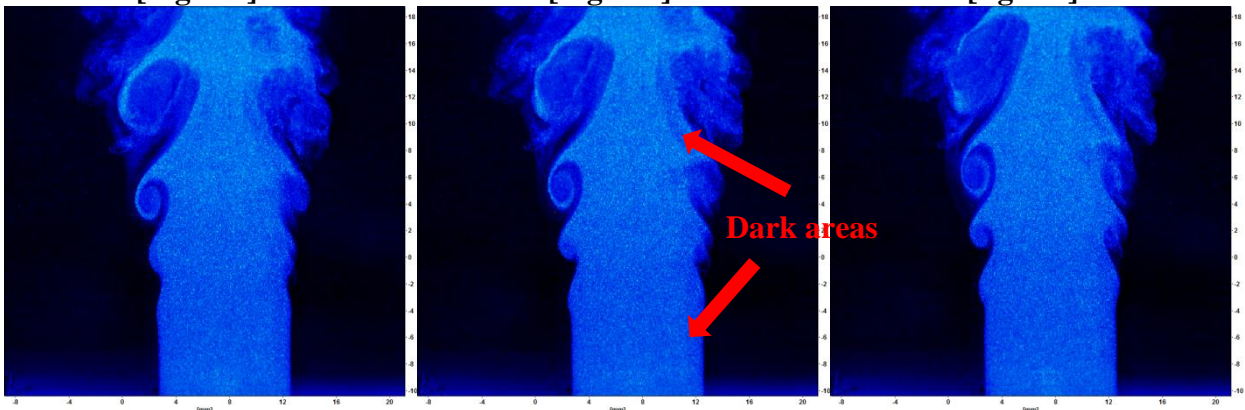


[fig 33d]

[fig 33e]

[fig 33f]

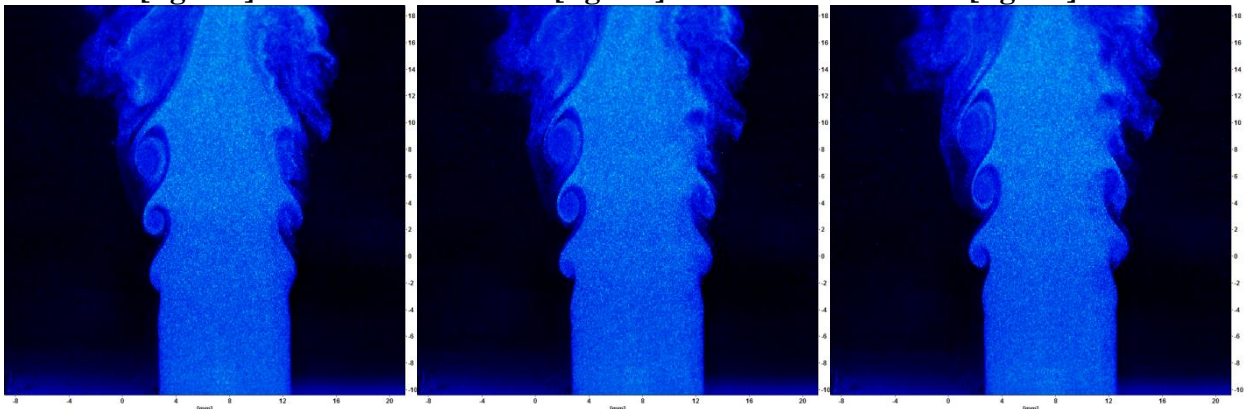


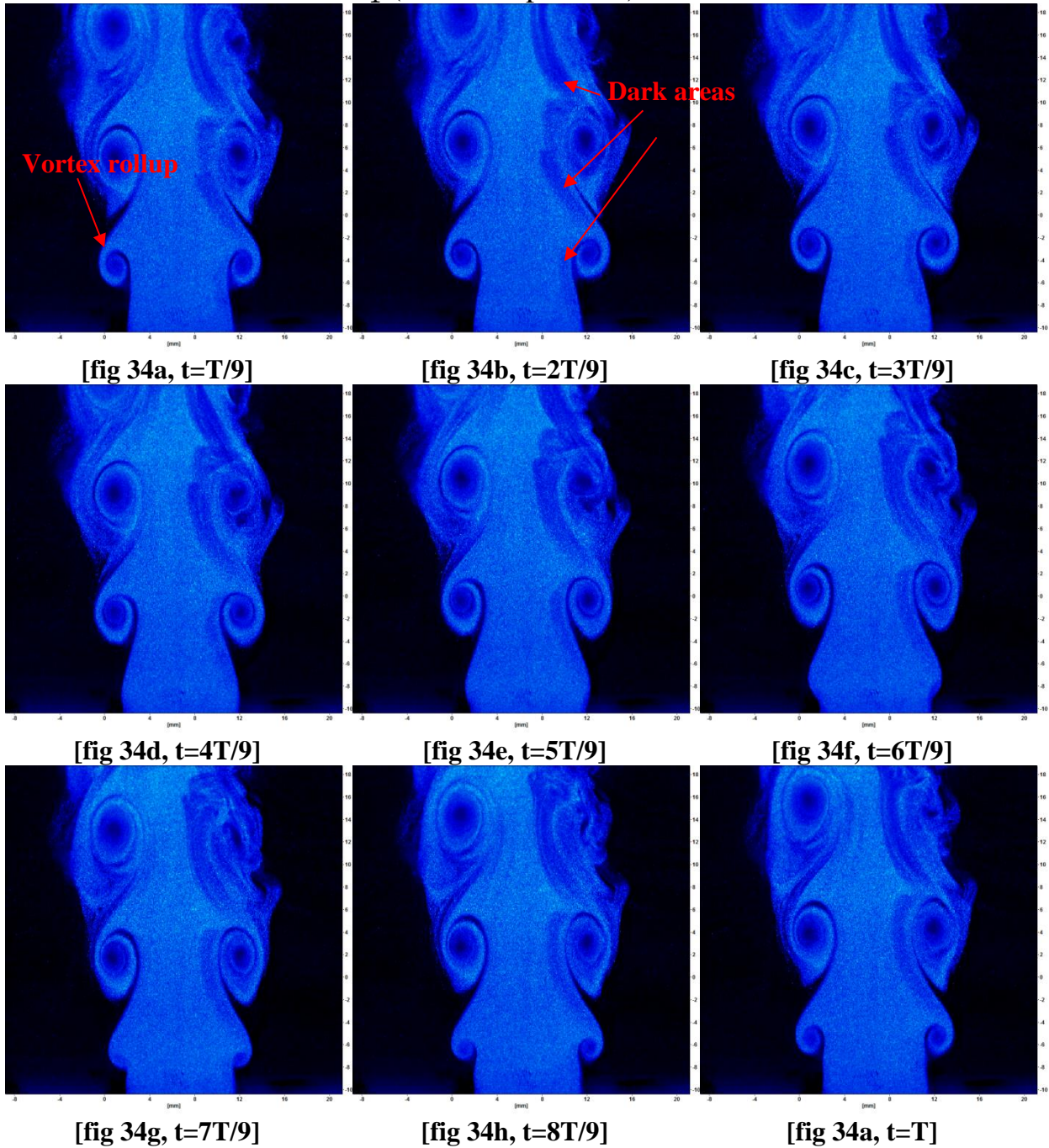
[fig 33g]

[fig 33h]

[fig 33i]

The unforced jet behaves pretty much as one would expect. There is a potential core in which the shape remains unchanged, until it begins rolling up and spreading, and turning into turbulent structures, as in figure 3. The dark areas that become more prominent in the forced jet are present here too, albeit much less visible.

P_1 (Antinode position)



At P_1 , the forcing is symmetric. This is reasonable to expect, as the acoustic field is also symmetric at the antinode position. There is a large dark area that develops with the vortices on the right side (red arrows, fig 34b). This is probably due to the same damage to the nozzle that causes the right side to break down faster.

$$P_2 = P_{ant} + \left(\frac{L}{4}\right) \frac{1}{5}$$

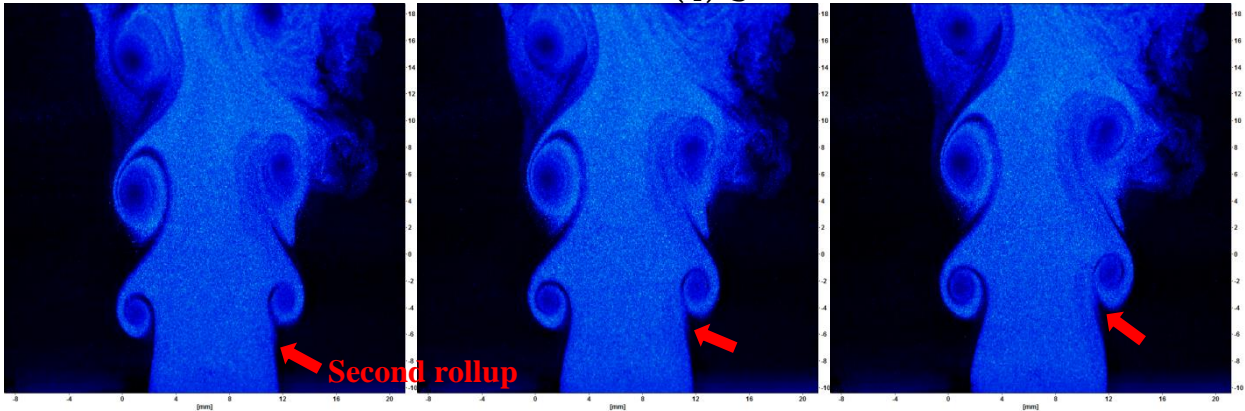


[fig 35a, $t=T/9$]

[fig 35b, $t=2T/9$]

[fig 35c, $t=3T/9$]

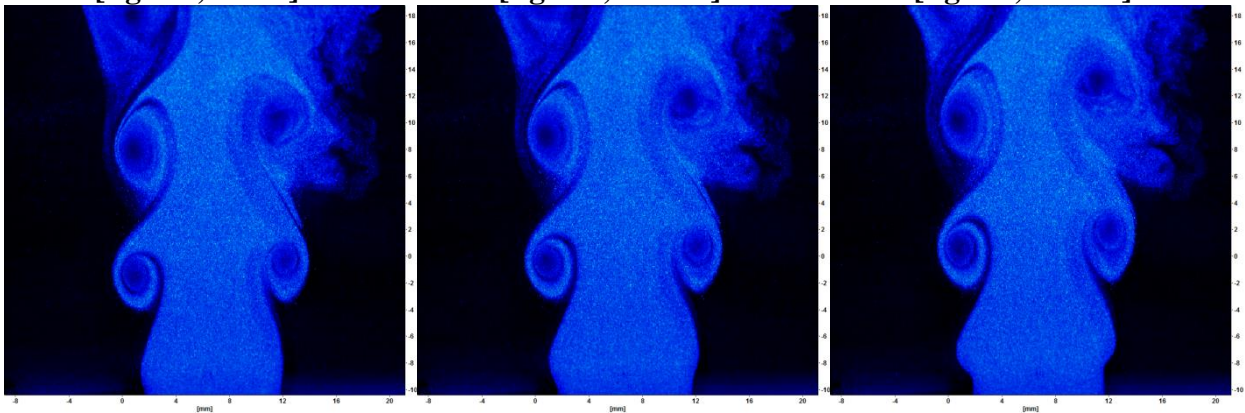


[fig 35d, $t=4T/9$]

[fig 35e, $t=5T/9$]

[fig 35f, $t=6T/9$]

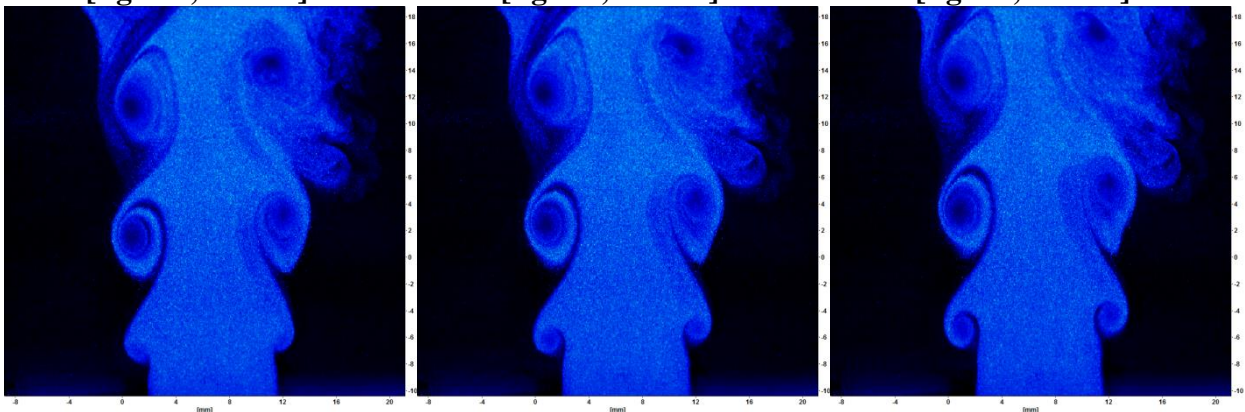


[fig 35g, $t=7T/9$]

[fig 35h, $t=8T/9$]

[fig 35i, $t=T$]

At P_2 , the roll up starts slightly faster on the left (node) side, but otherwise there is little visible difference. A second vortex rollup which becomes more prominent as the jet is moved toward the node, is visible as a minute bulge and rollup in figs 30a-c (red arrows).

$$P_3 = P_{ant} + \left(\frac{L}{4}\right) \frac{2}{5}$$

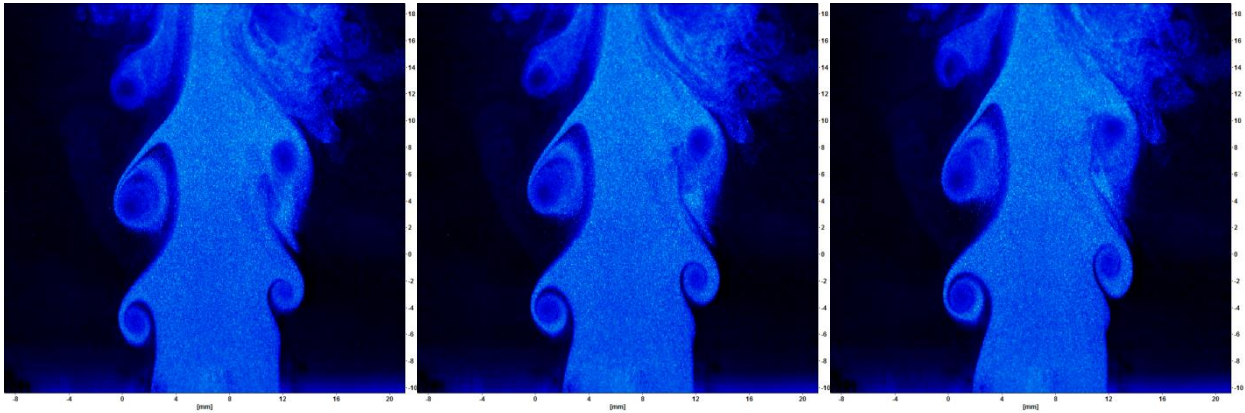


[fig 36a, $t=T/9$]

[fig 36b, $t=2T/9$]

[fig 36c, $t=3T/9$]

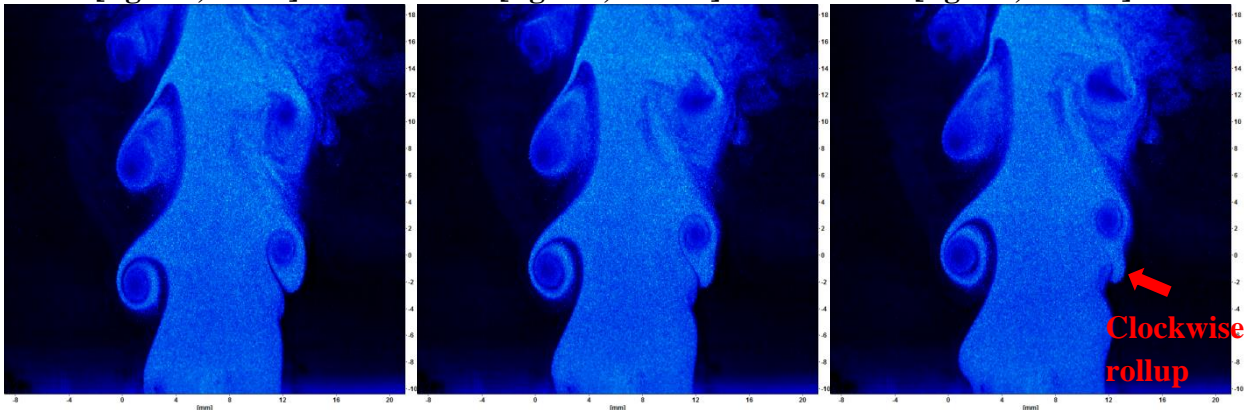


[fig 36d, $t=4T/9$]

[fig 36e, $t=5T/9$]

[fig 36f, $t=6T/9$]

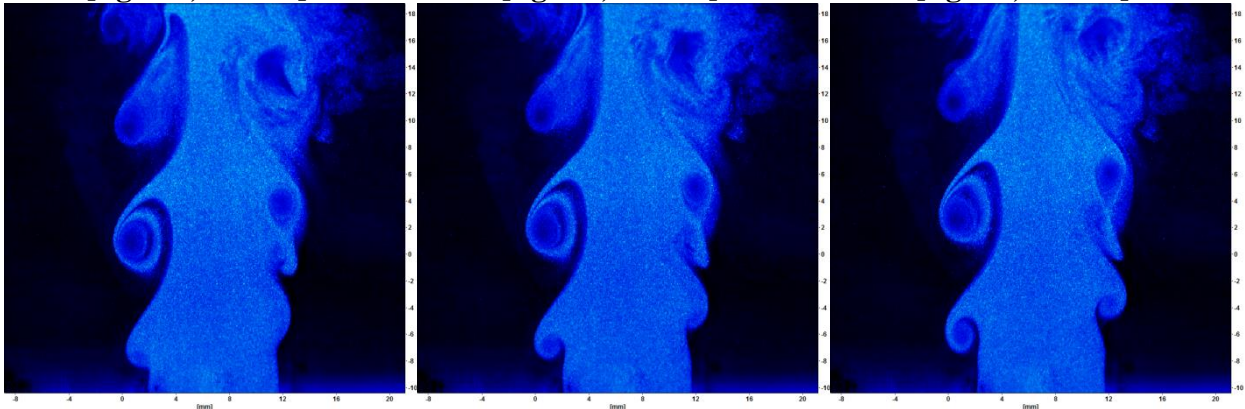


[fig 36g, $t=7T/9$]

[fig 36h, $t=8T/9$]

[fig 36i, $t=T$]

At P_3 , a trend begins to emerge as the first rollup becomes smaller and occurs earlier than in P_3 , while the second rollup becomes more prominent. It is now visible that it rolls up clockwise (most visible in 31f, red arrow), the same direction as the first rollup.

$$P_4 = P_{ant} + \left(\frac{L}{4}\right) \frac{1}{2}$$

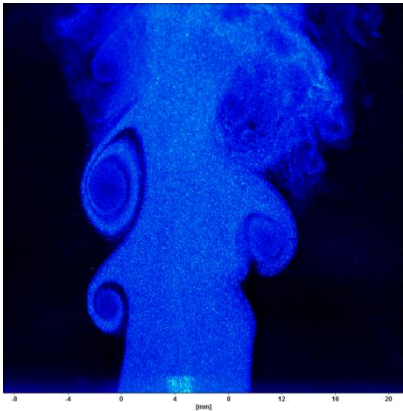


[fig 37a, $t=T/9$]

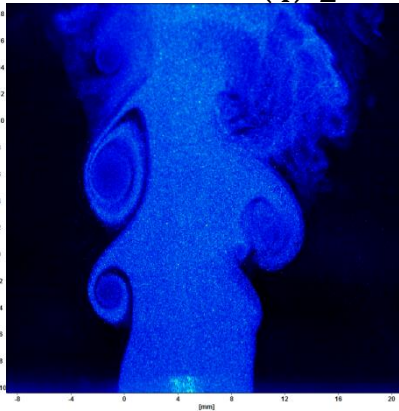


[fig 37b, $t=2T/9$]

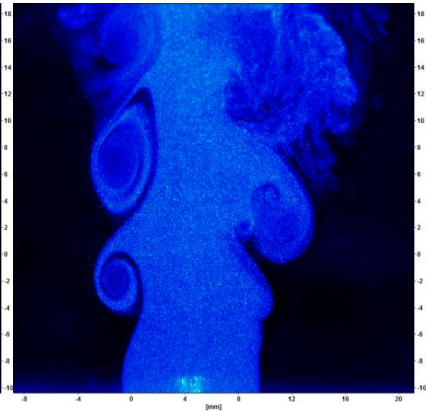


[fig 37c, $t=3T/9$]

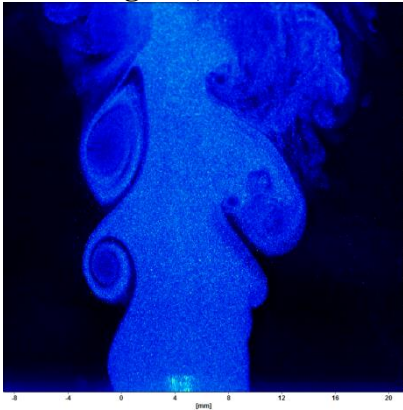


[fig 37d, $t=4T/9$]

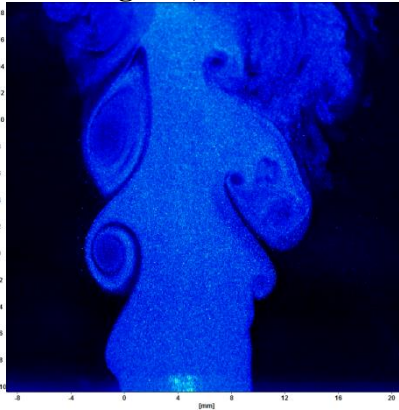


[fig 37e, $t=5T/9$]

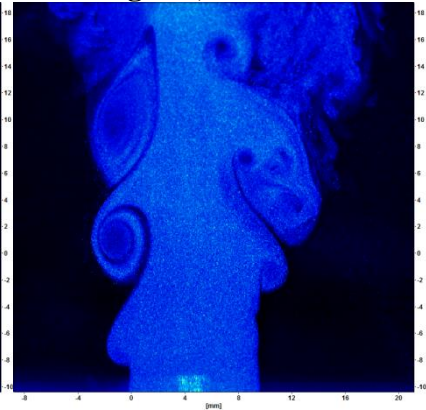


[fig 37f, $t=6T/9$]

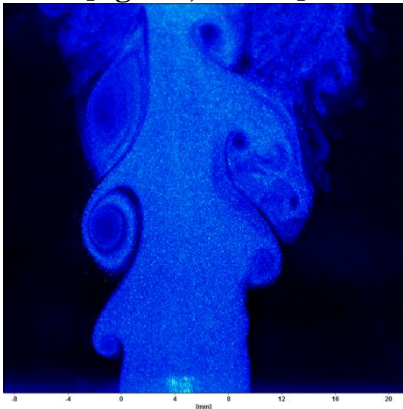


[fig 37g, $t=7T/9$]

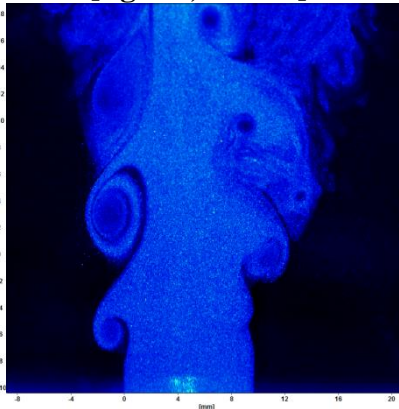


[fig 37h, $t=8T/9$]

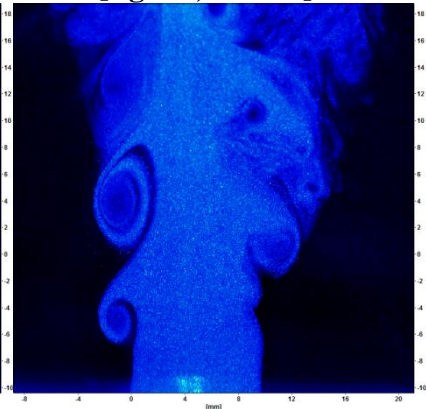


[fig 37i, $t=T$]

At P_4 the trend continues, where the first rollup keeps growing increasingly out of phase with its counterpart on the left side, and the second rollup increasing in strength.

$$P_5 = P_{ant} + \left(\frac{L}{4}\right)\frac{3}{5}$$

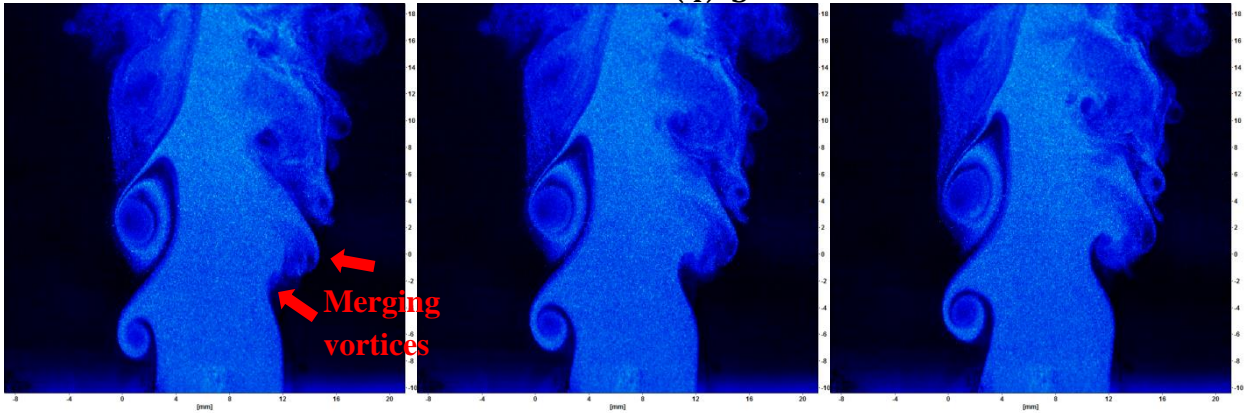


[fig 38a, $t=T/9$]

[fig 38b, $t=2T/9$]

[fig 38c, $t=3T/9$]

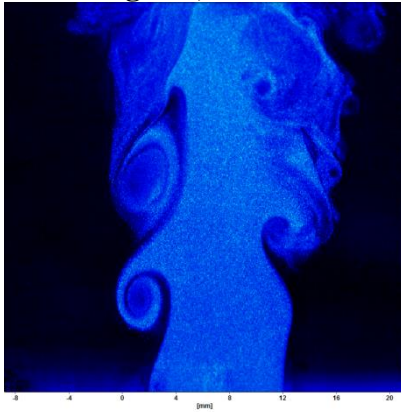


[fig 38d, $t=4T/9$]

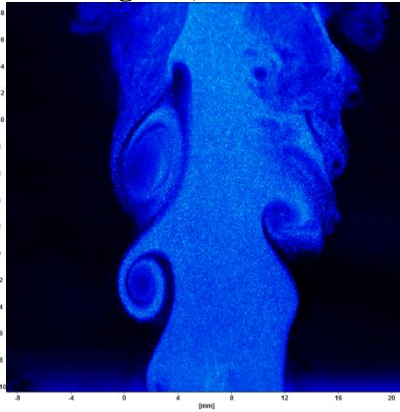


[fig 38e, $t=5T/9$]

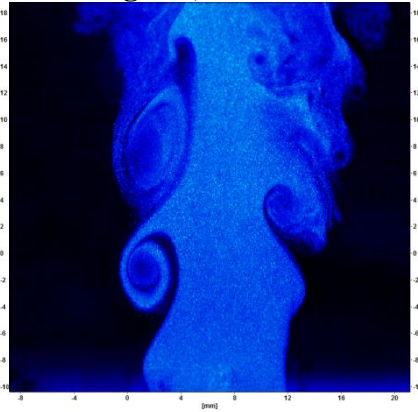


[fig 38f, $t=6T/9$]

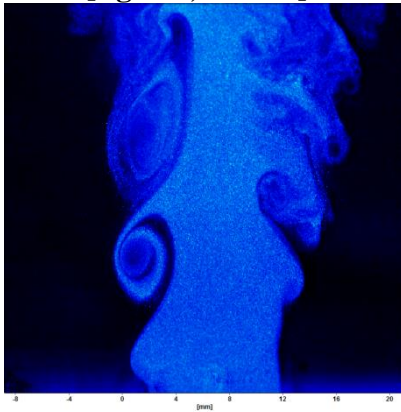


[fig 38g, $t=7T/9$]

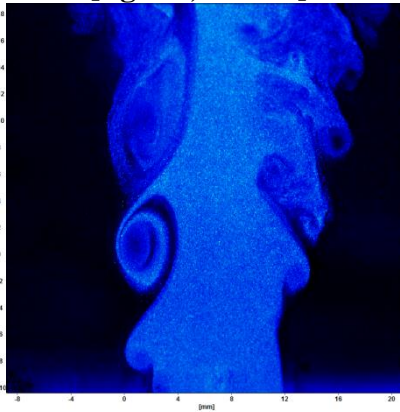


[fig 38h, $t=8T/9$]

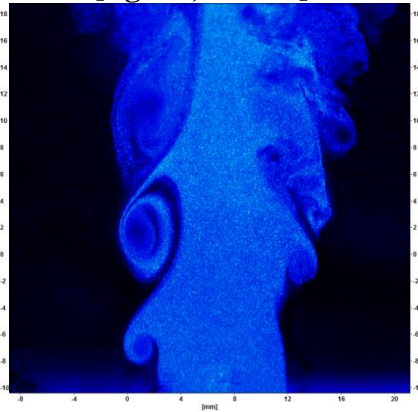


[fig 38i, $t=T$]

At P_5 , the first and second rollup begin to merge. They are still clearly distinct (red arrows pointing to each in fig 33a), however, and their action differs greatly from that on the left side.

$$P_6 = P_{ant} + \left(\frac{L}{4}\right)\frac{4}{5}$$

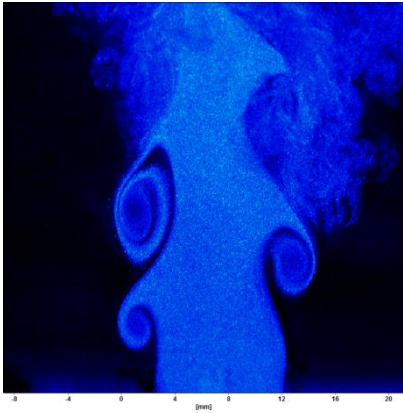


[fig 39a, $t=T/9$]

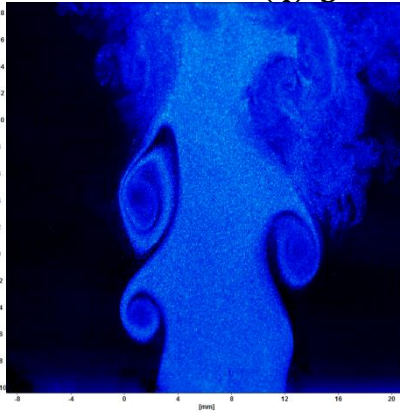


[fig 39b, $t=2T/9$]

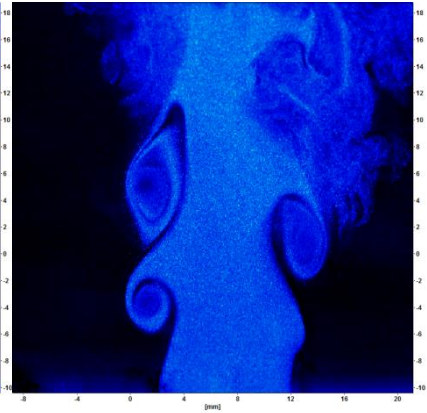


[fig 39c, $t=3T/9$]

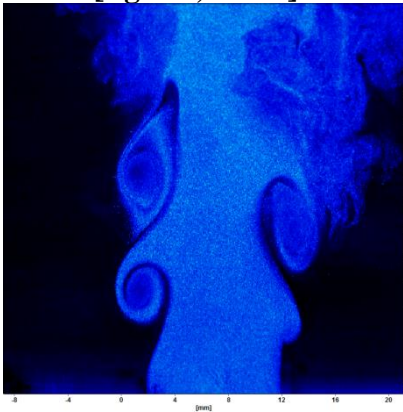


[fig 39d, $t=4T/9$]

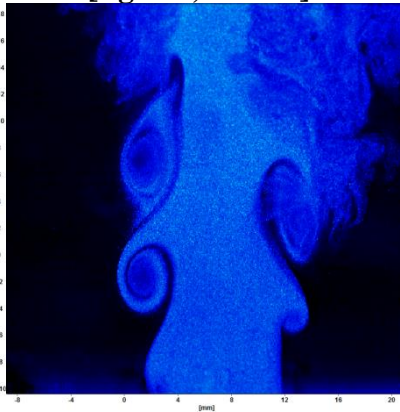


[fig 39e, $t=5T/9$]

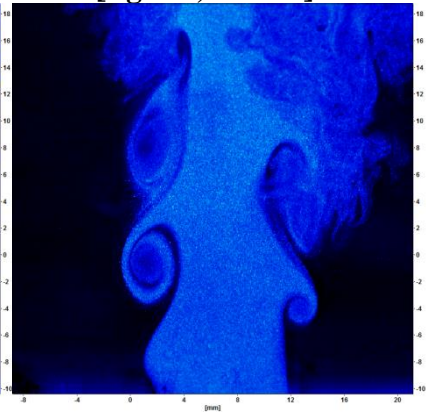


[fig 39f, $t=6T/9$]

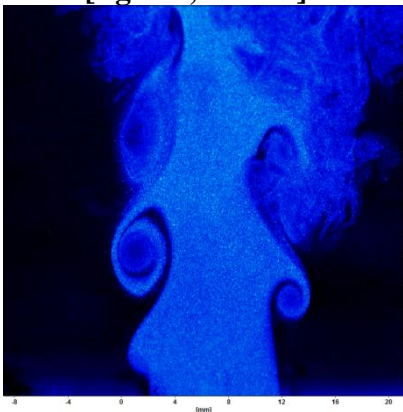


[fig 39g, $t=7T/9$]

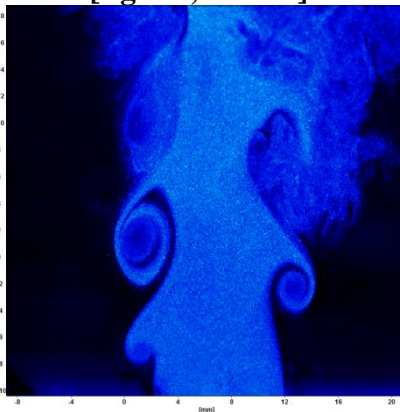


[fig 39h, $t=8T/9$]

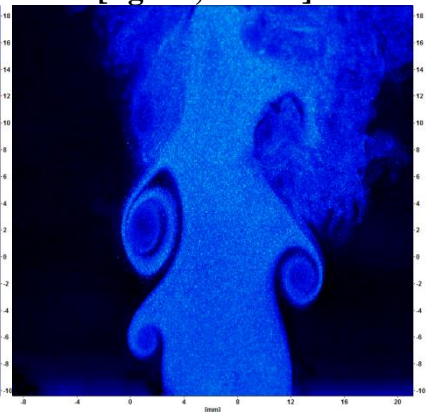


[fig 39i, $t=T$]

At P_6 , there is no longer a distinguishable first and second rollup on the right side.

$$P_7 = P_{ant} + \left(\frac{L}{4}\right) \text{Node position}$$

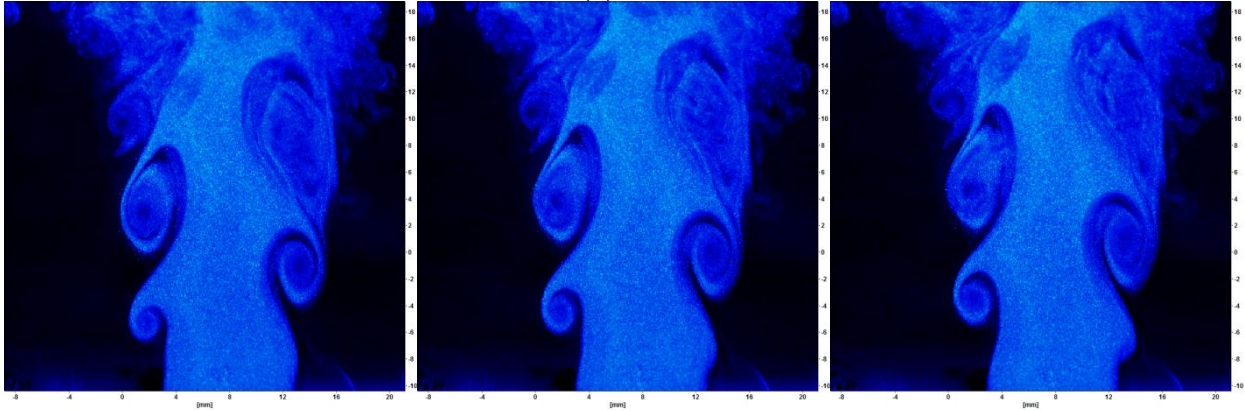


[fig 40a, $t=T/9$]

[fig 40b, $t=2T/9$]

[fig 40c, $t=3T/9$]

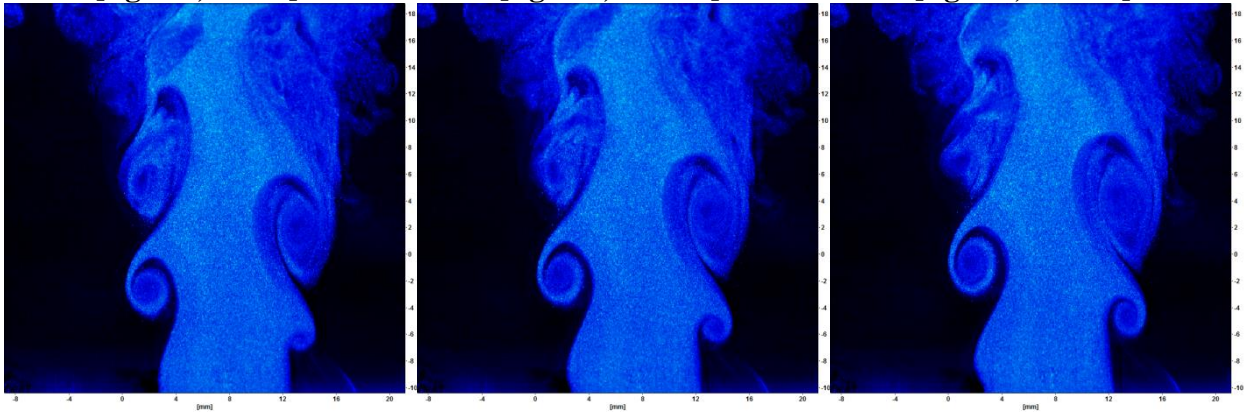


[fig 40d, $t=4T/9$]

[fig 40e, $t=5T/9$]

[fig 40f, $t=6T/9$]

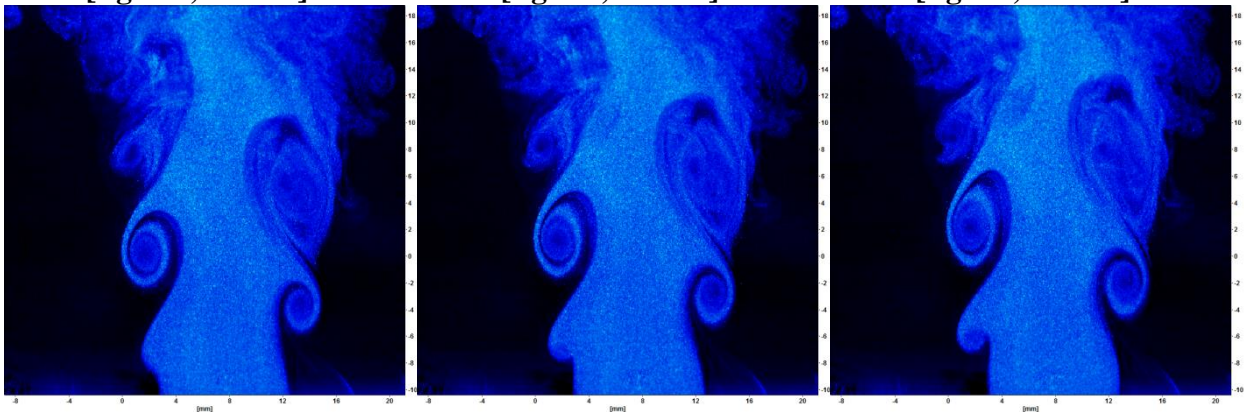


[fig 40g, $t=7T/9$]

[fig 40h, $t=8T/9$]

[fig 40i, $t=T$]

In the node at P_7 , the jet appears to be more or less antisymmetrical. Compared to P_6 , the rollup on the right side is stronger.

The appearance of the second vortex is somewhat unexpected. It indicates that there is a second mechanism by which the jet is modulated, or at least one that functions differently from that in the pressure antinode. A possible explanation might be in how the acoustic pressure and acoustic velocity both affect the jet. If so, however, it is clear that these effects are of a different nature, or else the middle (P_4) position would have vortices of equal strength.

This wouldn't be able to explain why the first rollup comes earlier and earlier compared to the antinode side. This also indicates that in addition to the mechanism of the second vortex being introduced, there are alterations in the original rollup mechanism.

It is also interesting that the rollup on the antinode side remains more or less unchanged. One could expect the antinode side to experience some of the changes the node side experiences as the jet is moved through, but it is not so. Whatever affects the node side, the antinode side appears to be shielded from it.

5. Conclusion

Throughout this thesis the acoustics of the chamber has been characterised and quantified, in order to get a good basis for the investigation of the jet in the acoustic field. This has not proved easy, and there is undoubtedly a thesis in itself properly documenting all the occurring modes, and their deviations from theory.

The experiment of the jet in the acoustic field has shown many interesting things. However, this thesis barely scratches the surface of what can be studied. The next logical step is proper PIV measurements, where much more quantitative data can be gathered and processed. The images captured are not ideal for PIV measurements; the capture is not directly phase-locked to the forcing, the images could be of better quality (reflections, glare, focus etc), and the box is not fully seeded. Some were nevertheless processed, as shown in fig 41. This particular image is a phase averaged image from the p3 position.

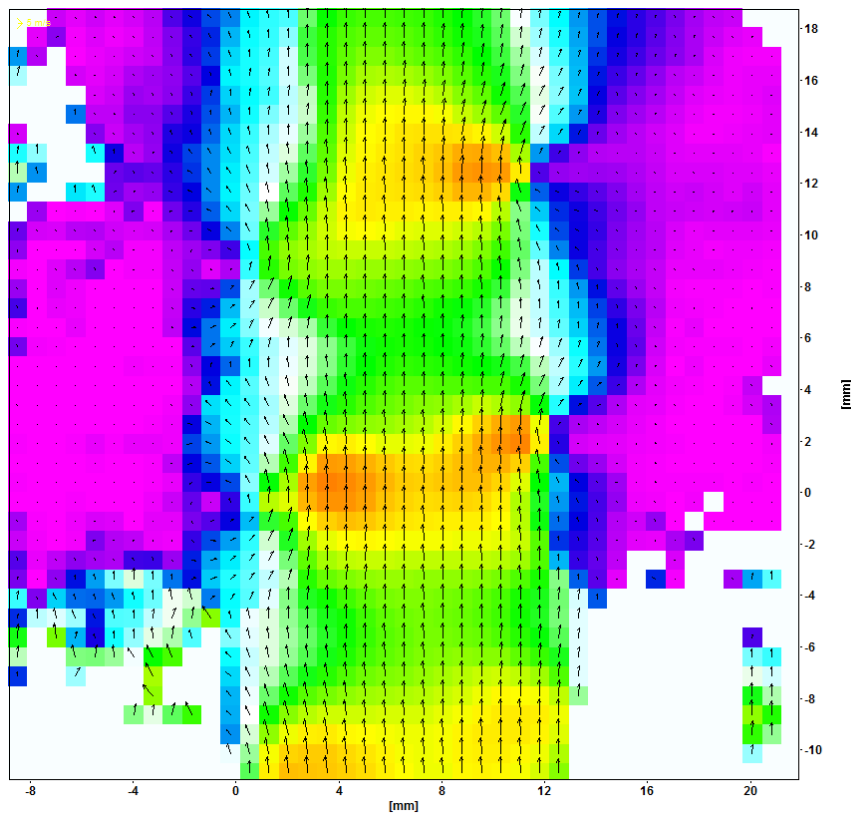


[fig 41: PIV example]

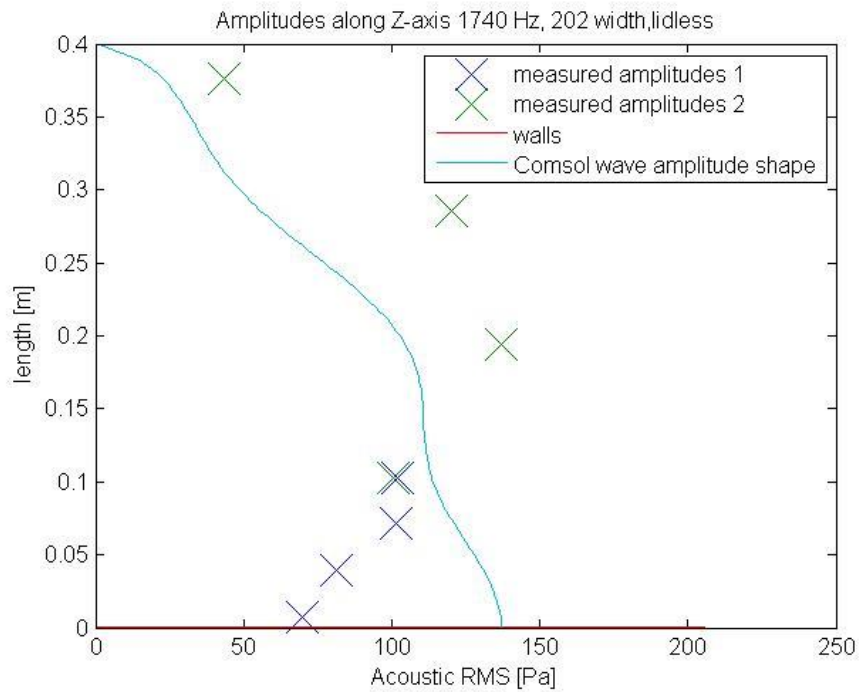
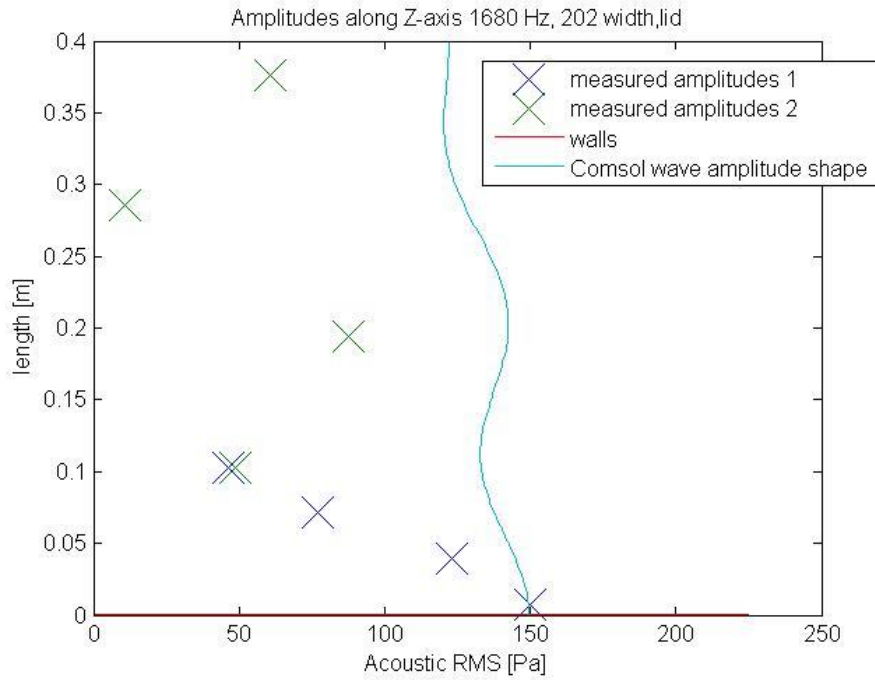
Even though the original goal of PIV measurements was not met, new insight has been gained, and hopefully, this thesis will be of some help on the road to fully understanding transversely forced jets.

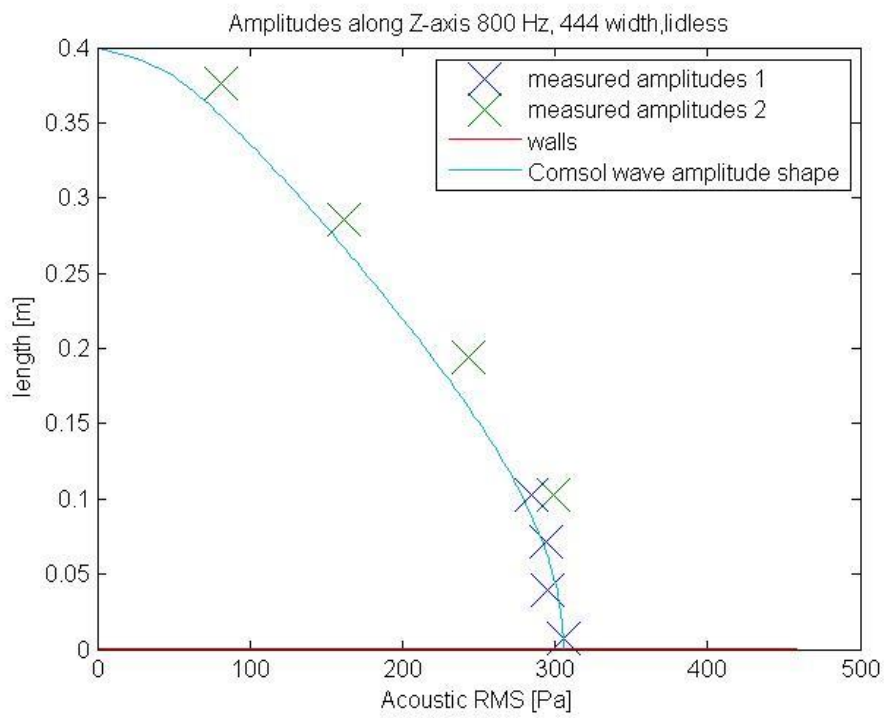
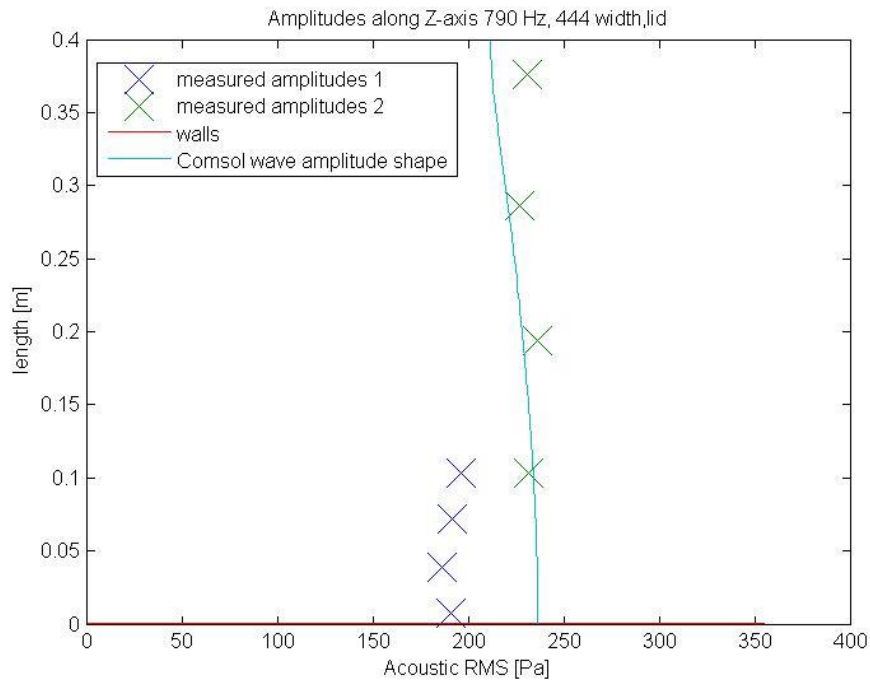
6. Bibliography

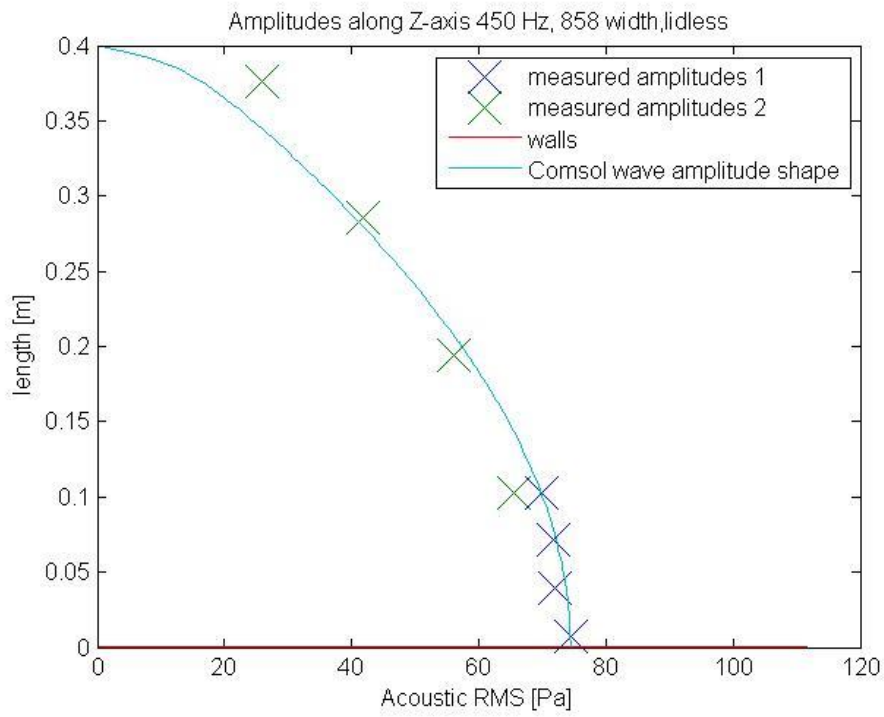
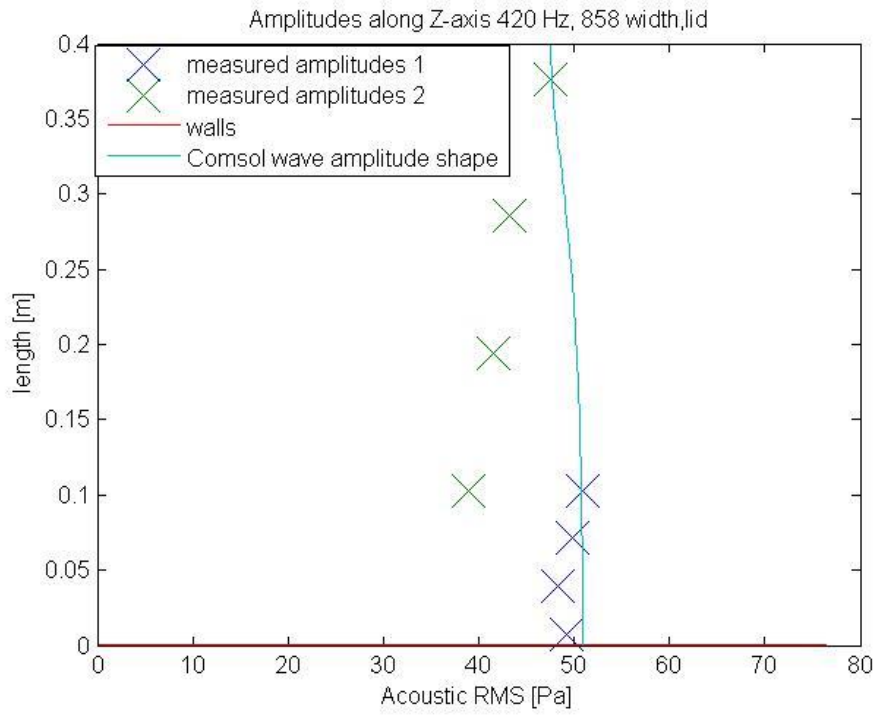
- [1] P. L. Rijke, "On the vibration of the air in a tube open at both ends," *Philosophical Magazine*, vol. 17, pp. 419-422, 1859.
- [2] F. Baillet and F. Lespinasse, "Response of a laminar premixed V-flame to a high-frequency transverse acoustic field," *Combustion and Flame*, 2013.
- [3] J. O'Connor and T. Lieuwen, "Recirculation zone dynamics of a transversely excited swirl flow and flame," *Physics of Fluids*, 2012.
- [4] A. Hirschberg and S. W. Rienstra, "An Introduction to Acoustics," 2005, pp. 18-19.
- [5] T. E. Vigran, "Building Acoustics," 2008, pp. 110-111.
- [6] S. C. Crow and F. H. Champagne, "Orderly structure in jet turbulence," *Journal of Fluid Mechanics*, 1971.
- [7] W. Reynolds, D. E. Parekh, P. Juvet and M. J. D. Lee, "Bifurcating and Blooming Jets," *Annual Review of Fluid Mechanics*, 2003.
- [8] M. Malanoski, M. Aguilar, V. Acharya and T. Lieuwen, "Dynamics of a transversely excited swirling, lifted flame," *Proceedings of ASME Turbo Expo 2013: Turbine Technical Conference and Exposition*, 2013.
- [9] A. Saurabh and C. Paschereit, "Combustion Instability in a Swirl Flow Combustor with Transverse Extensions," *Proceedings of ASME Turbo Expo 2013: Turbine Technical Conference and Exposition*, 2013.
- [10] F. Lespinasse, F. Baillet and T. Boushaki, "Responses of V-flames placed in an HF transverse acoustic field from a velocity to pressure antinode," 2013.
- [11] E. Kreyszig, *Advanced Engineering Mathematics*, Wiley, 2006.
- [12] M. Dalton, "Development of transversely forced jet apparatus," 2013.
- [13] D. Parekh, A. Leonard and W. C. Reynolds, "Bifurcating jets at high reynolds numbers," *Dep. Mech. Eng. Thermosci. Div. Rep.*.

Appendix

A.1 Z-axis plots with discrepancies







A.2 Pictures of the box and setup

